공학석사 학위논문

Supramolecular Systems for Photocatalytic Hydrogen Evolution from Water

광촉매 물분해 수소생산을 위한 초분자 시스템에 관한 연구

2016년 2월

서울대학교 대학원

재료공학부

김 동 하

Supramolecular Systems for Photocatalytic Hydrogen Evolution from Water

광촉매 물분해 수소생산을 위한 초분자 시스템에 관한 연구

지도 교수 박 수 영

이 논문을 공학석사 학위논문으로 제출함

2016 년 2 월

서울대학교 대학원

재료공학부 재료공학전공

김 동 하

김동하의 석사 학위논문을 인준함

2016 년 2 월

위 원 장 장 지 영 (인)

부위원장 박 수 영 (인)

위 원 안 철 희 (인)

Supramolecular Systems for Photocatalytic Hydrogen Evolution from Water

A THESIS SUBMITTED IN PARTIAL FULFILLMENT OF
THE REQUESTMENTS FOR THE DEGREE OF MASTER
IN ENGINEERING AT THE GRADUATE SCHOOL OF
SEOUL NATIONAL UNIVERSITY

FEBURARY 2016

By

Dongha Kim

Supervisor

Prof. Soo Young Park

Abstract

Supramolecular Systems for Photocatalytic Hydrogen Evolution from Water

Dongha Kim

Department of Materials Science and Engineering

The Graduate School

Seoul National University

As human civilization has grown larger, the use of fossil fuels has dramatically increased and severely harmed the earth. In addition to the environmental problems, limited fossil fuel reserves motivated people to search for new energy sources. In this context, there has been growing attention to artificial photosynthesis in order to produce renewable and environmentally-friendly energy sources. Natural photosynthesis in plants transforms solar energy into chemical fuel by synthesizing carbohydrate from water and carbon dioxide. Different from natural photosynthesis, artificial photosynthesis splits water into hydrogen and oxygen to use hydrogen as a chemical fuel (* This thesis limits the scope of artificial photosynthesis to water splitting). Hydrogen does not contain any carbon so that it only produces environmentally-friendly water as a byproduct during combustion. Also, as water produced in this way can be reused as a source of hydrogen, hydrogen energy is renewable. In pursuit of efficient and economical production of hydrogen, numerous approaches have been made. Particularly,

there has been a growing attention to supramolecular approach in order to improve the efficiency of photocatalytic system. By using supramolecular approach, we can modulate the photochemical properties of photocatalytic systems, and thus enhance their photocatalytic activity compared with the monomer counterparts.

This thesis covers two novel supramolecular systems for photocatalytic hydrogen evolution from water. In Chapter 2, I report on the first self-healing system which spontaneously repairs molecular catalyst during photocatalytic hydrogen evolution. A bipyridine-embedded UiO-type metal-organic framework (MOF), namely Pt_n_Ir_BUiO, which incorporates H_2-evolving catalyst and photosensitizer was synthesized and subject to photocatalytic hydrogen evolution reaction. Though embedded in MOF, each molecular species could maintain their intrinsic properties because the functionalized MOF system worked as a supramolecular system. Photocatalytic hydrogen evolution with $Pt_{0.1}$_Ir_BUiO showed very stable molecular photocatalysis without significant decrease in its activity and colloidal formation for 6.5 days at least; in homogeneous counterpart, the molecular catalyst became Pt colloid just after 7.5 h. It was revealed that the arrangement of diimine sites which closely and densely surround the H_2-evolving catalyst in the MOF enabled such a highly efficient self-healing.

In Chapter 3, an amphiphilic Ir(III) complex was synthesized and shown to form supramolecular assembly in water via hydrophobic collapse. Interestingly, when sodium chloride salt was added to induce the charge screening effect, electrostatic repulsion between self-assembled structures became weaker and the solution became a hydrogel. More importantly, this hydrogel was effective for photocatalytic hydrogen evolution as it could incorporate all necessary components such as water, photosensitizer, catalyst, and sacrificial reducing agent.

Keywords: Artificial photosynthesis, Water splitting, Photocatalytic hydrogen evolution, Self-healing, Metal-organic framework, Self-assembly, Ir(III) complex, Hydrogel
Student Number: 2014-20535

Contents

List of Abbreviations

ACT	acetone
DCM	dichloromethane
DMA	*N*,*N*´-dimethylaniline
DMF	*N*,*N*´-dimethylformamide
DMSO	dimethylsulfoxide
h	hour
HOMO	highest occupied molecular orbital
HRMS	high-resolution mass spectrometry
LUMO	lowest unoccupied molecular orbital
M	mole(s) per liter
MC	metal centered
MeCN	acetonitrile
MLCT	metal to ligand charge transfer
PHEMD	Photo-Hydrogen-Evolving Molecular Device
PS	photosensitizer
SR	sacrificial reducing agent
TEA	triethylamine
THF	tetrahydrofuran
TLC	thin layer chromatography
TOF	turnover frequency
TON	turnover numbers

WRC	water reduction catalyst

List of Tables

List of Schemes

List of Figures

Chapter 1. Introduction

1.1 Artificial photosynthesis

Plants transform solar energy into chemical fuel through photosynthesis. The energy they accumulated in the earth has served as food resources for animals or as a power source for human civilization. Photosynthesis is conducted by chloroplast located inside of plant leaves. Its thylakoid membrane contains protein machineries that conduct sequent process of light absorption, charge transfer and catalysis, thus completing the photosynthesis cycle. The photosynthesis cycle allows plants to convert water and carbon dioxide into carbohydrates which have served as various forms of energy sources needed for the creatures living on the earth.

On the other hand, as human civilization has grown larger, the use of fossil fuels has dramatically increased and harmed the earth. In addition to environmental problems, the limited fossil fuel reserves motivated people to search for new energy sources. In this context, there has been growing attention to artificial photosynthesis in order to produce renewable and environmentally-friendly energy sources. Different from natural photosynthesis, artificial photosynthesis splits water into hydrogen and oxygen to use hydrogen as a chemical fuel. Hydrogen does not contain any carbon, and it only produces environmentally-friendly water as a byproduct during combustion. Also, water produced in this way can be reused as a

source of hydrogen, and thus hydrogen energy is renewable. Hydrogen is an ideal fuel as it is not only eco-friendly and renewable, but also has high energy density of 120 MJ/kg.

1.2 Principle of photocatalytic hydrogen evolution

Hydrogen is produced through water reduction which is one of the two half-reactions in water splitting. Especially, when light energy is used for the reaction, it is called photocatalytic hydrogen evolution. It is performed by photosensitizer (PS), water reduction catalyst (WRC), and sacrificial reducing agent (SR). Basically, PS converts light energy to electrochemical energy, SR provides electron for PS, and WRC produces one hydrogen by reducing two protons. When PS absorbs light, one of its electron in HOMO goes to LUMO and it becomes PS^*. In reductive quenching mechanism as described in Figure 1.1a, PS^* takes one electron from SR and becomes PS^-. By giving its excited electron to WRC, PS^- returns to its original state and WRC reduces protons to produce hydrogen. In oxidative quenching mechanism as described in Figure 1.1b, PS^* gives its excited electron to WRC and becomes PS^+. While WRC reduces protons to produce hydrogen, SR gives one electron to PS^+ and it returns to its original state. The efficiency of photocatalytic hydrogen evolution is determined by 1) how efficient PS is in converting the light energy into electrochemical energy, i.e., PS^*, 2) the rate of electron transfer from SR to PS and PS to WRC, and 3) the catalytic efficiency of WRC.

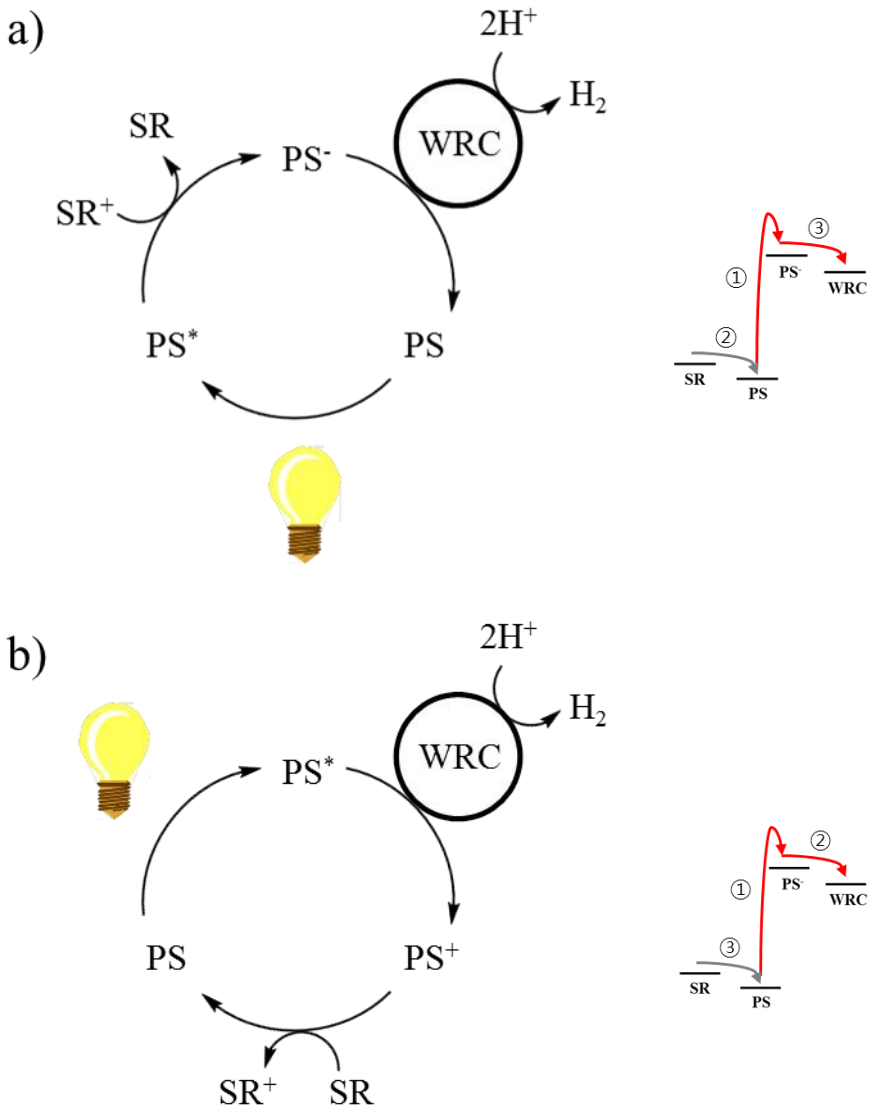

Figure 1.1 The principle of photocatalytic water reduction. a) Reductive quenching mechanism. b) Oxidative quenching mechanism.

1.3 Ir(III) complexes as PS

Ir(III) and Ru(II) complexes have widely been used as PS in photocatalytic hydrogen evolution (Figure 1.2).[1] They have high visible light absorption, long lifetime of excited electron, and thermodynamically high driving force to deliver their excited electrons to WRC.[2] Moreover, the photochemical properties of these complexes can be modulated by altering their ligands to adjust the energy level of their excited electron.[1] Thus, if we know the reduction potential of a WRC, we can systematically design a suitable PS and enable efficient charge transfer between WRC and PS. However, in case of Ru(II) complexes, their photochemical stability is limited by the bond cleavage between Ru(II) center and ligand during photocatalysis.[3] The occupation of excited electron into their MC orbital (anti-bonding orbital) is thermally available, and thus weakens their photochemical stability. In contrast, such occupation is rarely possible in Ir(III) complexes because they have large energy gap between the energy level of their excited electron and that of their MC orbital. In addition, Ir(III) photosensitizers usually follow reductive quenching mechanism in which excited electron is readily transferred to WRC (Figure 1.1a), while Ru(II) photosensitizers follow oxidative quenching mechanism (Figure 1.1b) which can cause back electron transfer.[2] For these reasons, Ir(III) complexes have shown higher efficiency than Ru(II) complexes.[1] In addition, some Ir(III) complexes showed exceedingly high stability in terms of TON. Bernhard group reported an Ir(III)

complex which contains two pyridine groups in its ancillary ligand. This pyridine groups could adsorb to the surface of Pt colloid and promoted efficient charge transfer between the Ir(III) complex and Pt colloid during photocatalytic hydrogen evolution (It recorded 8800 TON).[4] In my group, we recently synthesized an Ir(III) complex which contains triphenylsilyl (TPS) group in its ancillary ligand. TPS group enhanced the robustness of the Ir(III) complex by its steric effect, and it recorded 17000 TON in combination with Pt colloid.[5]

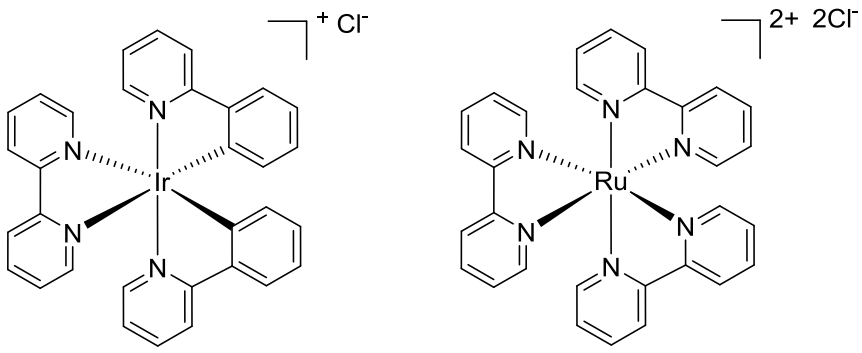

Figure 1.2 Basic structure of Ir(III) and Ru(II) complexes. $[Ir(ppy)_2(bpy)]^{+}\cdot Cl^{-}$ (left, ppy represents phenylpyridine and bpy represents bipyridine) and $[Ru(bpy)_3]^{2+}\cdot 2Cl^{-}$ (right).

1.4 Pt(II) complexes and Pt(0) colloid as WRC

The use of transition-metal complexes as WRC allows us to systematically design their properties through ligand tuning, and thus achieve high photocatalytic efficiency. Many research on Rh(III)-, Pt(II)-, Co (II)- or (III)-, and Fe(I)-based complexes revealed that they have photocatalytic activities as WRC.[6-10] Among them, Sakai group used various Pt(II) complexes for photocatalytic hydrogen evolution and showed that they are highly efficient WRCs (Figure 1.3).[9] However, one implication is that the Pt(II) molecular catalysts are prone to undergo degradation in the photolysis conditions, and more importantly, they sometimes act as precursors for colloidal metal catalysts.[8,11-13] Although colloidal catalysts, such as Pt(0) or Pd(0) colloids, sometimes show high catalytic activities, they have intrinsic weak points in achieving tunability and selectivity. In this regard, preventing transformation of the molecular catalysts into metal colloids would be an important step towards artificial photosynthesis.

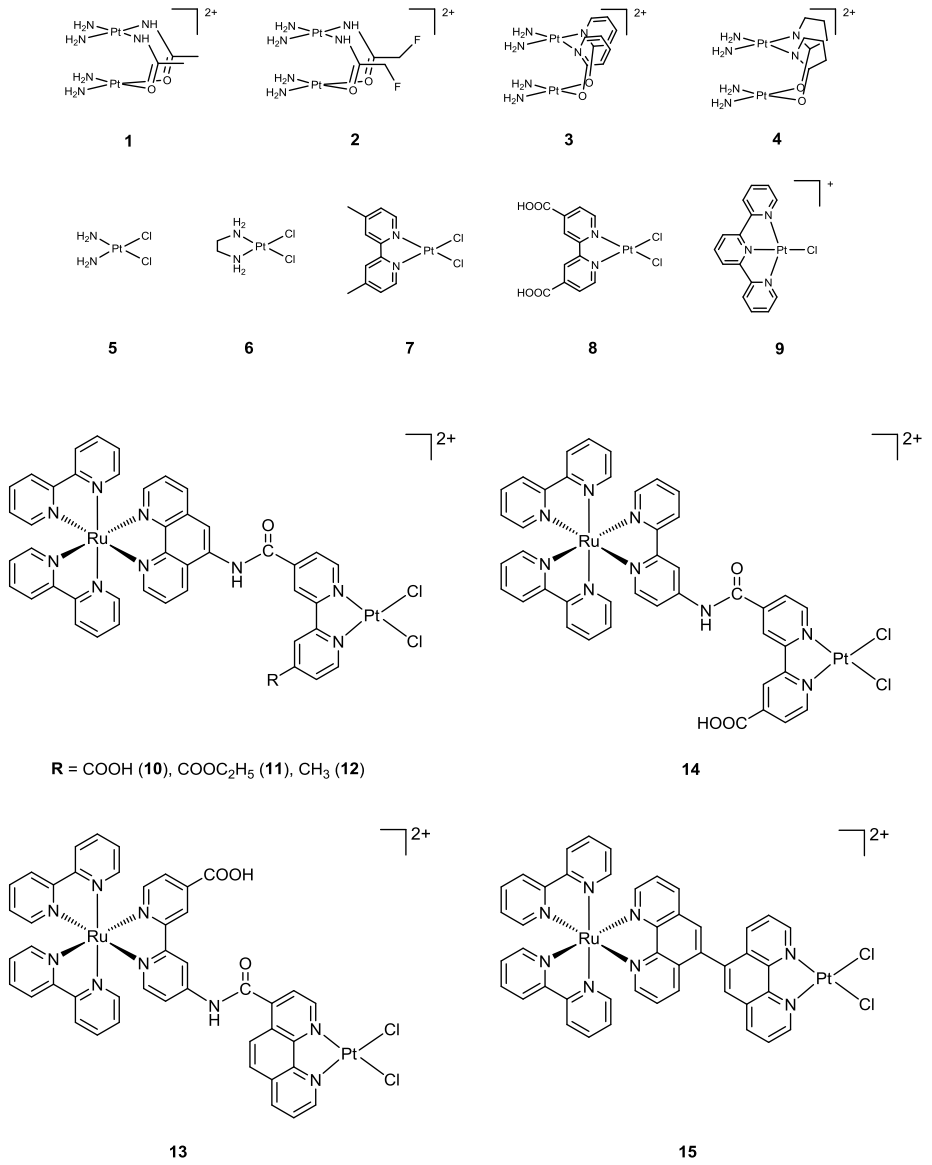

Figure 1.3 Various Pt(II) complexes for photocatalytic hydrogen evolution (**1**–**9**), some of them are covalently connected to Ru(II) photosensitizer to enhance their photocatalytic activity (**10**–**15**).[9]

1.5 Supramolecular system

To enhance the efficiency of photocatalytic hydrogen evolution, supramolecular approach has drawn wide attention. Supramolecular system is referred to the chemical systems made up of functional molecular subunits which are connected to each other. Though covalently connected, their intrinsic properties are retained as their electronic coupling is small. The advantage of using such system in artificial photosynthesis is that the distance between PS and WRC can be effectively shortened to enhance their charge transfer while maintaining each of their functions. As depicted in Figure 1.4, covalently connected PS and WRC can proceed a desired photocatalysis when they form supramolecular assembly. However, if their electronic coupling is so large that they lose their own properties, they become just a large molecule and cannot conduct a desired photocatalysis. In Sakai's group, as shown in Figure 1.3, they covalently attached Pt(II) catalyst to Ru(II) photosensitizer to make **10**–**15** and showed that the complexes functioned as supramolecular systems with far enhanced photocatalytic efficiency.[9]

Metal-organic frameworks (MOFs) are solid compounds consisting of metal clusters (secondary building units) and organic linkers which are connected with each other and form a reticular structure (Figure 1.5). MOFs are highly porous, chemically stable, and some of them are even robust in water. More importantly, the incorporation of functionalized organic linker into MOFs is readily available without altering the functions of the organic linker and the

crystallinity of the MOFs. There have recently been some approaches to enhance the efficiency of photocatalytic system by using MOF as a supramolecular system.[14-21] Several MOF systems were synthesized and used as photocatalytic systems, showing far more enhanced stability and activity than homogeneous counterparts. Metal clusters or organic linkers in the MOFs were functionalized to make them work as PS or WRC (Figure 1.6). Despite of their heterogeneous nature, almost all active sites in the MOF systems could participate in the photocatalysis because of the MOF's high porosity. Also, the proximity between PS and WRC ensured their efficient charge transfer.

The term, supramolecular system, is also referred to the chemical systems in which molecular species interact with each other via non-covalent bonding, forming an assembled structure as shown in Figure 1.7. Based on this concept, some approaches have been made towards photocatalytic hydrogen evolution and the resulting supramolecular systems were shown to work efficiently.

A typical method is to use low-molecular weight gelators (LMWGs). LMWGs can form one- or two-dimensional self-assembly in water and create hydrogel systems. The self-assembly often brings about new photochemical property to the system, such as excitonic coupling, and enhances the photocatalytic efficiency. In addition, quantum efficiency of hydrogel systems can be improved because the vibration of molecule is restricted in gel state, which thus lessens non-radiative decay.[23,24] Stupp's group, for example, designed a PMI-based charged amphiphilic chromophore which can

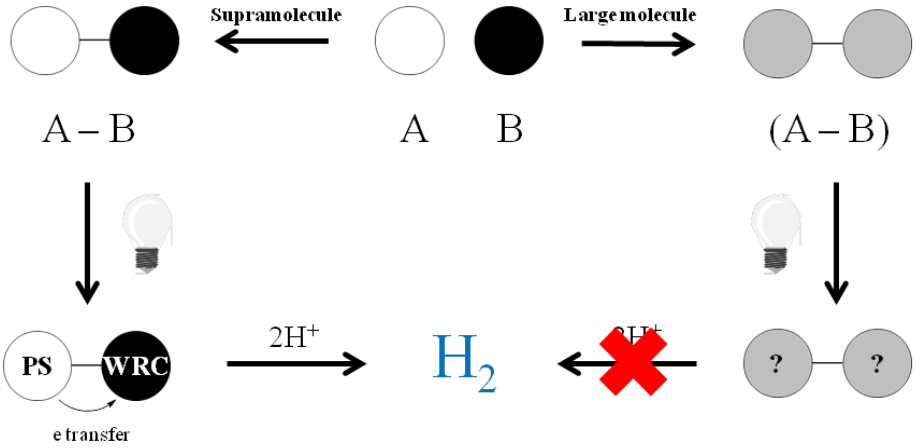

Figure 1.4 Supramolecular system in which intrinsic properties of each species are not changed.

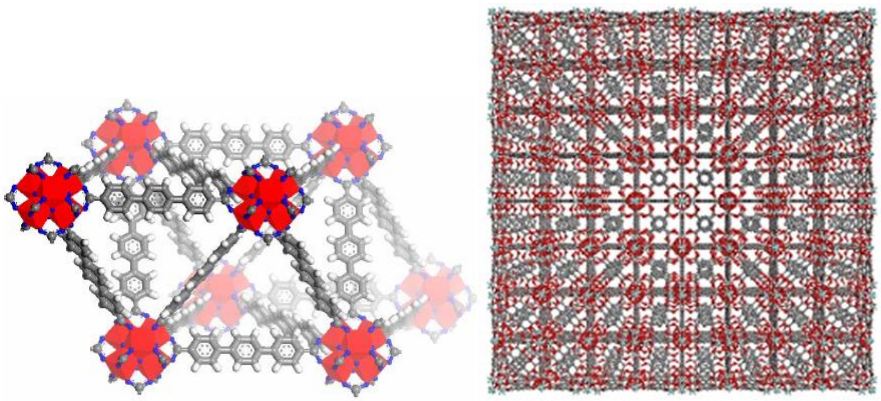

Figure 1.5 The reticular structure of MOF system (UiO-type MOF).[22]

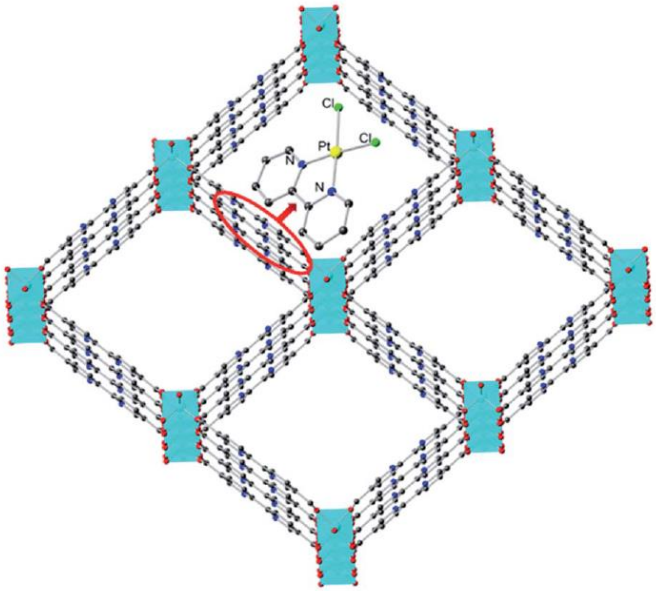

Figure 1.6 Modification of MOF-253 with $PtCl_2$.[18]

self-assemble two-dimensionally in water due to hydrophobic collapse (Figure 1.8). Importantly, the resulting assembly had the alignment of transition dipoles extended across a number of molecules, and thus enabled the exciton to spread out over multiple molecules. Also, the exciton produced in this assembly represented a high potential-energy state that could be utilized to drive electron transfer for photocatalytic process.[25]

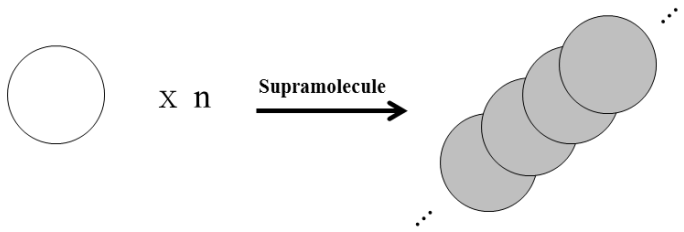

Figure 1.7 Intermolecular interaction through non-covalent bonding forming a supramolecular system.

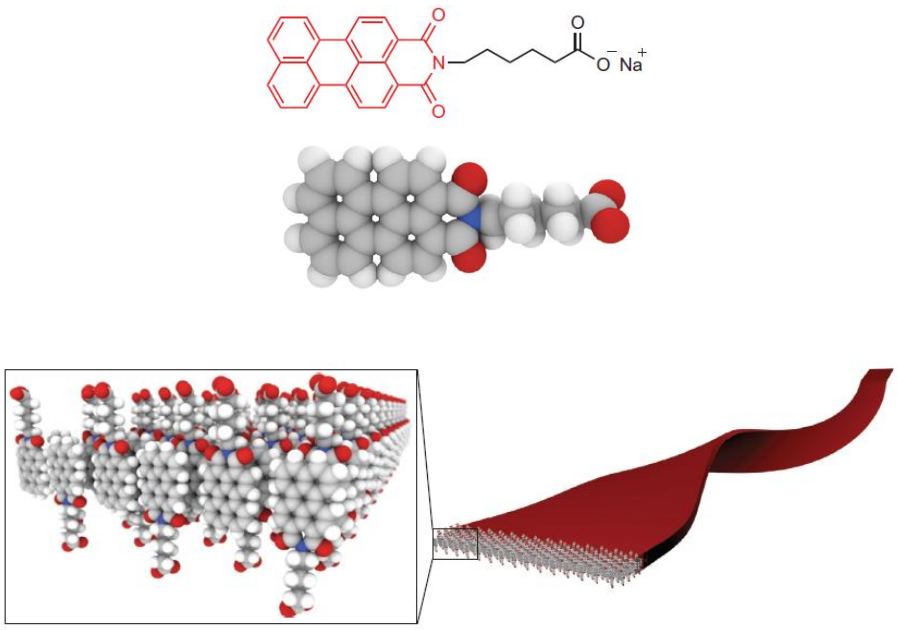

Figure 1.8 A 2-D supramolecular ribbon as gelation moiety of PMI-hydrogel.[25]

1.6 References

1. J. I. Goldsmith, W. R. Hudson, M. S. Lowry, T. H. Anderson, S. Bernhard, *J. Am. Chem. Soc.* **2005**, *127*, 7502.
2. Na, M. Wang, J. Pan, P. Zhang, B. Å kermark, L. Sun, *Inorg. Chem.* **2008**, *47*, 2805.
3. L. L. Tinker, N. D. McDaniel, S. Bernhard, *J. Mater. Chem.* **2009**, *19*, 3328.
4. B. F. DiSalle; S. Bernhard *J. Am. Chem. Soc.* **2011**, *133*, 11819.
5. D. R. Whang; K. Sakai; S. Y. Park *Angew. Chem.* **2013**, *125*, 11826.
6. Guttentag, M.; Rodenberg, A.; Kopelent, R.; Probst, B.; Buchwalder, C.; Brandstätter, M.; Hamm, P.; Alberto, R. *Eur. J. Inorg. Chem.* **2012**, *2012*, 59.
7. Du, P.; Eisenberg, R. *Energy Environ. Sci.* **2012**, *5*, 6012.
8. Eckenhoff, W. T.; Eisenberg, R. *Dalton Trans.* **2012**, *41*, 13004.
9. Ozawa, H.; Sakai, K. *Chem. Commun.* **2011**, *47*, 2227.
10. Thoi, V. S.; Sun, Y.; Long, J. R.; Chang, C. J. *Chem. Soc. Rev.* **2013**, *42*, 2388.
11. Artero, V.; Fontecave, M. *Chem. Soc. Rev.* **2013**, *42*, 2338.
12. Pfeffer, M. G.; Schafer, B.; Smolentsev, G.; Uhlig, J.; Nazarenko, E.; Guthmuller, J.; Kuhnt, C.; Wachtler, M.; Dietzek, B.; Sundstrom, V.; Rau, S. *Angew. Chem. Int. Ed.* **2015**, *54*, 5044.
13. Du, P.; Schneider, J.; Li, F.; Zhao, W.; Patel, U.; Castellano, F. N.; Eisenberg, R. *J. Am. Chem. Soc.* **2008**, *130*, 5056.

14. Hansen, R. E.; Das, S. *Energy Environ. Sci.* **2014**, *7*, 317.
15. Meyer, K.; Ranocchiari, M.; van Bokhoven, J. A. *Energy Environ. Sci.* **2015**.
16. Nasalevich, M. A.; Becker, R.; Ramos-Fernandez, E. V.; Castellanos, S.; Veber, S. L.; Fedin, M. V.; Kapteijn, F.; Reek, J. N. H.; van der Vlugt, J. I.; Gascon, J. *Energy Environ. Sci.* **2014**, *8*, 364.
17. Wen, M.; Mori, K.; Kamegawa, T.; Yamashita, H. *Chem. Commun.* **2014**, *50*, 11645.
18. Zhou, T.; Du, Y.; Borgna, A.; Hong, J.; Wang, Y.; Han, J.; Zhang, W.; Xu, R. *Energy Environ. Sci.* **2013**, *6*, 3229.
19. Pullen, S.; Fei, H.; Orthaber, A.; Cohen, S. M.; Ott, S. *J. Am. Chem. Soc.* **2013**, *135*, 16997.
20. Wang, C.; deKrafft, K. E.; Lin, W. *J. Am. Chem. Soc.* **2012**, *134*, 7211.
21. Zhang, Z. M.; Zhang, T.; Wang, C.; Lin, Z.; Long, S.; Lin, W. *J. Am. Chem. Soc.* **2015**.
22. Cavka, J. H.; Jakobsen, S.; Olsbye, U.; Guillou, N.; Lamberti, C.; Bordiga, S.; Lillerud, K. P. *J. Am. Chem. Soc.* **2008**, *130*, 13850.
23. Tam, A. Y.; Yam, V. W. *Chem. Soc. Rev.* **2013**, *42*, 1540.
24. Okeyoshi, K.; Yoshida, R. *Chem. Commun.* **2011**, *47*, 1527.
25. Weingarten, A. S.; Kazantsev, R. V.; Palmer, L. C.; McClendon, M.; Koltonow, A. R.; Samuel, A. P.; Kiebala, D. J.; Wasielewski, M. R.; Stupp, S. I. *Nat. Chem.* **2014**, *6*, 964.

Chapter 2. Self-Healing of Catalysts on Metal-Organic Framework: Highly-Robust Molecular System for Photocatalytic Hydrogen Evolution from Water

2.1 Introduction

In natural photosystem II (PSII), plants incorporate manganese-based molecular catalyst within their lipid matrix for highly efficient solar-to-fuel conversion.[1] In this context, there have been numerous approaches of using transition metal complexes as molecular photosensitizer and catalyst to mimic the efficient light-harvesting and solar-to-fuel conversion.[2-4] One implication is that the molecular catalysts prone to undergo degradation in the photolysis conditions, and more importantly, they sometimes act as precursors for colloidal metal catalysts.[5-8] Although the colloidal catalysts, such as Pt or Pd colloids, often show high catalytic activities, they have intrinsic weak points in achieving tunability and selectivity. In this regard, preventing transformation of the molecular catalysts into metal colloids would be an important step towards artificial photosynthesis.

To circumvent the low stability of molecular catalysts and prevent unwanted transformation into metal colloids, using self-healing platform that

continuously repairs molecular catalysts would be a promising approach. Inspired by the self-repair mechanism of PSII in plants, Nocera group developed a heterogeneous cobalt catalyst which can repair itself by using phosphate counterion.[9] However, there has been no report on self-healing systems for molecular catalyst so far. Eisenberg group reported regeneration of damaged molecular H_2-evolving catalyst by excessively adding the ligand molecule that constitutes the catalyst.[10,11] Despite few fold increase in the catalyst's lifetime, the system was material-consuming and less systematic to be termed as 'self-healing'.

Metal-organic framework (MOF) has merits of high porosity and easy functionalization, thus can provide unique means to engineer molecular catalysis in heterogeneous systems.[12-16] More importantly, integration of different functional units in one platform guaranteed proximity between them to boost mutual charge and energy transfer.[17-19] Also, each molecular species could maintain their intrinsic properties because functionalized MOF systems worked as supramolecular systems. In this context, molecular catalysts and photosensitizers were embedded in water-stable MOFs for photocatalytic hydrogen evolution and they showed far more enhanced activity and stability than homogeneous counterparts.[20-22] As an additional step forward, I herein report an original strategy for self-healing MOF that not only proceeds photocatalytic hydrogen evolution, but also spontaneously repairs molecular catalyst during the photocatalytic process. Water-stable bipyridine-embedded UiO-67 MOF, namely BUiO, was selected as a self-healing solid platform and was functionalized with Pt(II) catalyst and Ir(III) photosensitizer to yield

Pt_n_Ir_BUiO (Scheme 2.1). The reticular structure of the MOF would arrange a number of diimine sites nearby the molecular catalyst and facilitate re-bonding of broken metal–diimine bond during photocatalysis.

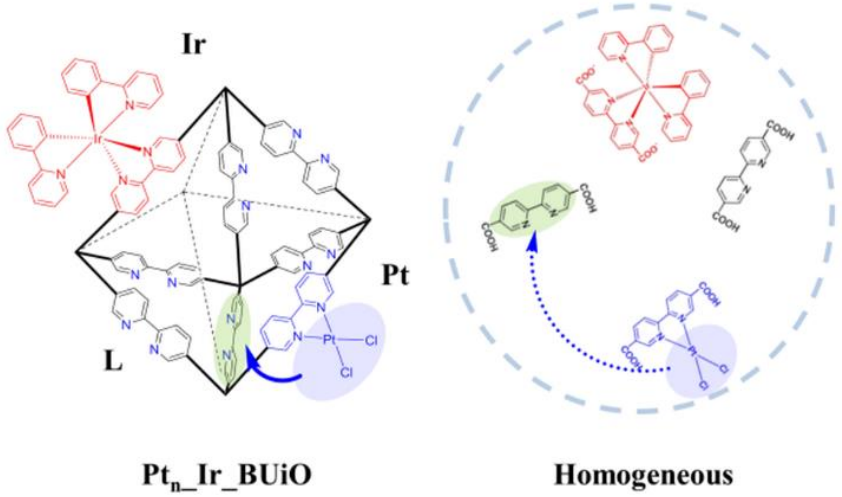

Scheme 2.1 Schematic operation principle of self-healing MOF (Pt_n_Ir_BUiO) and the corresponding homogeneous system.

2.2 Experimental section

General Methods

Commercially available chemicals were purchased from Sigma-Aldrich, Acros, and Alfa Aesar, unless otherwise noted, and used as received. All glasswares and magnetic stirring bars were thoroughly dried in an oven (60 ℃). Reactions were monitored using thin layer chromatography (TLC). Commercial TLC plates (silica gel 254, Merck Co.) were developed and the spots were visualized under UV light at 254 or 365 nm. Silica gel column chromatography was performed with silica gel 60G (particle size 5-40 μm, Merck Co.). ^{1}H NMR spectra were collected with a Bruker AVANCE-300 NMR spectrometer. Chemical shifts (δ) are given in ppm and referenced to TMS. High-resolution mass spectrometry (HRMS) spectra were recorded on a JMS-700 MStation (JEOL). Powder X-ray Diffraction (PXRD) patterns were collected on a Bruker New D8 Advance. Cu Kα radiation was used. The simulated pattern of BUiO single-crystal diffraction was achieved from CCDC 968930. Inductively coupled plasma-mass spectroscopy (ICP-MS) data were obtained with ELAN 6100, Perkin-Elmer SCIEX and all samples were analyzed three times and averaged (mean). Field emission scanning electron microscope (FE-SEM) images and energy-dispersive x-ray spectroscopy (EDS) data were acquired on a JEOL, JSM-6700F microscope and high resolution transmission electron microscope (HR-TEM) images were

acquired on a JEOL, JEM-3010.

Synthesis of $[Ir(ppy)_2(L)]^-Na^+ \cdot 1.5H_2O$ (Na^+Ir)

$[Ir(ppy)_2(\mu\text{-}Cl)]_2$ was synthesized according to the literature procedure.[23] $[Ir(ppy)_2(\mu\text{-}Cl)]_2$ (500 mg) and 2,2'-bipyridine-5,5'-dicarboxylic acid (274 mg) were dispersed in 50 ml ethylene glycol. The mixture was stirred at 150 ℃ for 4 h under Ar atmosphere. The crude product was cooled to room temperature and put dropwise into water. Resulting suspension was washed with water, filtered, and dried overnight in vacuum oven at 60 ℃. Dried solid was dispersed in methanol and droplets of 0.3N NaOH were added until the solution becomes clear. The resulting solution was evaporated and purified using a silica gel column chromatography with MeOH and the mixed solution of MeOH:MC 1:1 v/v as eluents, followed by reprecipitation in acetone.

Red solid, Yield: 402 mg (52 %). ^{1}H NMR (300 MHz, D_2O) δ 8.61 (d, J = 8.4 Hz, 2H), 8.45 (dd, J = 8.4, 2.1 Hz, 2H), 8.42 (s, 2H), 8.10 (d, J = 8.0 Hz, 2H), 7.92 – 7.81 (m, J = 14.9, 7.9 Hz, 4H), 7.70 (d, J = 5.3 Hz, 2H), 7.12 (t, J = 7.1 Hz, 2H), 7.02 (t, 2H), 6.98 (t, 2H), 6.44 (d, J = 7.4 Hz, 2H). Anal. Calcd for $C_{34}H_{25}IrN_4NaO_{5.5}$: C, 51.5%; H, 3.18%; N, 7.07%, Found: C, 51.7%; H, 3.16%; N, 6.88%. Energy-dispersive x-ray spectroscopy (EDS) measurement of the Ir complex showed Na/Ir ratio of 1.05.

Synthesis of $Pt(H_2L)Cl_2$ (H_2Pt)

The synthesis of H_2**Pt** was slightly modified from the literature method.[24] Zeise's salt (104 mg) and 2,2'-bipyridine-5,5'-dicarboxylic acid (60 mg) were dispersed in 3.5 ml MeOH. The mixture was stirred at 45 ℃ for 30 min under Ar atmosphere. The crude product was washed with MeOH, filtered, and dried overnight in vacuum oven at 60 ℃.

Red brown solid, Yield: 98 mg (74 %). ^{1}H NMR (500 MHz, DMSO) δ 10.01 (d, J = 1.7 Hz, 2H), 8.81 (dd, J = 8.3, 1.8 Hz, 2H), 8.76 (d, J = 8.4 Hz, 2H); HRMS (FAB, positive) m/z 473.9825 ($[M\text{-}Cl^-]^+$; calcd.: 473.9820). In place of MeOH, DMF as a solvent with same procedure also resulted in the same product.

Synthesis and Characterization of Ir_BUiO

Synthesis of Ir_BUiO was performed by mixed ligand synthesis. Mixture of $ZrCl_4$ (55.5 mg), 2,2'-bipyridine-5,5'-dicarboxylic acid (H_2**L**, 45 mg), and $[Ir(ppy)_2(\mathbf{L})]^-Na^+ \cdot 1.5H_2O$ (Na^+**Ir**, 15.5 mg) was subject to solvothermal reaction in the solution of 7.5 ml DMF, 550 μl acetic acid, and 388 μl water. The programmed temperature control was referred to the reported procedure; 80 ℃ for 12h, heating to 120 ℃ for 30 min, and maintaining 120 ℃ for 24 h.[25] The resulting solid with apricot color was filtered and washed with DMF thoroughly. The remaining solvents were removed in dynamic vacuum at 130 ℃ for 4 h, followed by soaking in acetone for 3 days (3 refreshes, yield : 88 %). After the soaking and filtration, MOF was dried in vacuum at room temperature. The PXRD result shows that the structure of Ir_BUiO is in

accordance with the mother complex, BUiO (Figure 2.3). Deprotonated ancillary ligand of iridium complex, **L** in $[Ir(ppy)_2(\mathbf{L})]^-Na^+$, would induce integration of iridium complex into MOF as a linker rather than as a guest molecule inside the pore of MOF due to the strong interaction between anionic **L** and cationic zirconium cluster.[26]

Post-Synthetic Metalation (PSM) of Ir_BUiO

Mixing H_2**Pt**, Na^+**Ir**, and H_2**L** together for mixed-ligand synthesis transformed H_2**Pt** into Pt colloid during solvothermal reaction. Thus, I introduced post-synthetic metalation (PSM) with Zeise's salt for functionalization of Ir_BUiO with Pt. PSM was done in DMF with Ir_BUiO by referring to the synthesis of H_2**Pt**. The reaction conditions are very mild lasting only 80 min, thus minimizing harmful effects on Ir_BUiO. When using MeOH instead of DMF the product was less-crystalline due to harmful effect of MeOH on BUiO.[27]

$Pt_{0.8}$_Ir_BUiO : Zeise's salt (3.2 mg) was dissolved in 4 ml DMF and Ir_BUiO (32 mg) was added, followed by sonication. The mixture was stirred at 45 ℃ for 80 min under Ar atmosphere. The crude product was filtered and washed with DMF and acetone, and resulting solid was soaked in acetone for 3 days (3 refreshes). Remaining acetone was removed by drying in vacuum (Yield: 90 %).

$Pt_{0.2}$_Ir_BUiO : Zeise's salt (0.64 mg) was dissolved in 4 ml DMF, and following procedures were equal to those of $Pt_{0.8}$_Ir_BUiO (Yield: 85 %).

$Pt_{0.1}$_Ir_BUiO : Zeise's salt (0.32 mg) was dissolved in 4 ml DMF, and following procedures were equal to those of $Pt_{0.8}$_Ir_BUiO (Yield: 88 %).

Chemical composition of MOF systems

The composition of each MOF was determined by energy-dispersive x-ray spectroscopy (EDS), inductively coupled plasma mass-spectrometer (ICP-MS), and ^{1}H-NMR. The relative amounts of each element in MOF were calculated by EDS and ICP-MS (Figure 2.1). The ratio of O/Zr and N/Zr and Cl/Pt ratio almost coincided with the theoretical values (Table 2.1), certifying the successful PSM.

The loading amounts of **Pt** and **Ir** in $Pt_{0.8}$_Ir_BUiO were calculated with ICP-MS. For ICP-MS measurement, $Pt_{0.8}$_Ir_BUiO (3 mg) was dissociated in 0.3N NaOH (2.5 ml) by sonication and vortex. Resulting solution was atomized in nitric acid hydrochloride and analyzed with dilution. Amounts of Pt and Ir were analyzed three times and averaged (mean). Consequently, the amounts of **Pt** and **Ir** in MOF were found to be 0.37 and 0.45 μmol, respectively. Similarly, the amounts of **Pt** and **Ir** in 3 mg of $Pt_{0.2}$_Ir_BUiO were calculated as 0.043 μmol and 0.28 μmol, respectively, and 0.029 μmol and 0.30 μmol for $Pt_{0.1}$_Ir_BUiO.

Next, I took ^{1}H NMR experiment to quantify the ratio of **L** to metal

complexes. I dissociated Ir_BUiO in 0.3N NaOH D_2O solution to remove each component from the MOF. After removing precipitates, such as ZrO_2, ^1H NMR measurement was taken. The spectra in Figure 2.2 showed that hydrogen peaks of **Ir** (red circles) were same as those of pristine Na^+**Ir** which exclude the possibility of degradation of **Ir** during MOF synthesis and the calculated molar ratio of **L** to **Ir** was 10. The **L** to **Ir** ratio of $Pt_{0.8}$_Ir_BUiO was not changed from that of Ir_BUiO during PSM and soaking in acetone. However, **Pt** was impossible to be measured by NMR because it precipitated in NaOH solution. In combination with the ICP-MS data, total ratio of each species in $Pt_{0.8}$_Ir_BUiO was determined as **Pt** : **Ir** : **L** = 0.8 : 1 : 10. The compositions of $Pt_{0.2}$_Ir_BUiO (**Pt** : **Ir** : **L** = 0.16 : 1 : 10) and $Pt_{0.1}$_Ir_BUiO (**Pt** : **Ir** : **L** = 0.1 : 1 : 10) were also determined according to the same procedure.

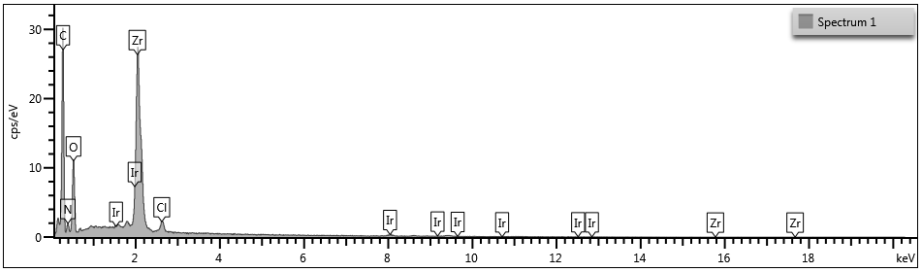

Figure 2.1 EDS measurement of $Pt_{0.8}$_Ir_BUiO. The sample was attached on carbon tape and measured after Pt coating (peaks corresponding to Pt were removed from the data).

Table 2.1 EDS measurement of $Pt_{0.8}$_Ir_BUiO.

	theoretical	measured
O/Zr	5.33	3.95
N/Zr	2	1.84[b]
Ir/Zr	-	0.0382
Pt/Ir	ICP-MS data : 0.81[a]	
Pt/Zr	-	0.0309
Cl/Zr	-	0.0964
Cl/Pt	2	1.88[c]

a. Pt/Ir ratio was calculated with ICP-MS because Pt coating on the sample hampered the exact measurement of Pt amount

b. The amount of N which belongs to the cyclometalating ligands of Ir was subtracted

c. The amount of Cl which is the counter ion of Ir was subtracted

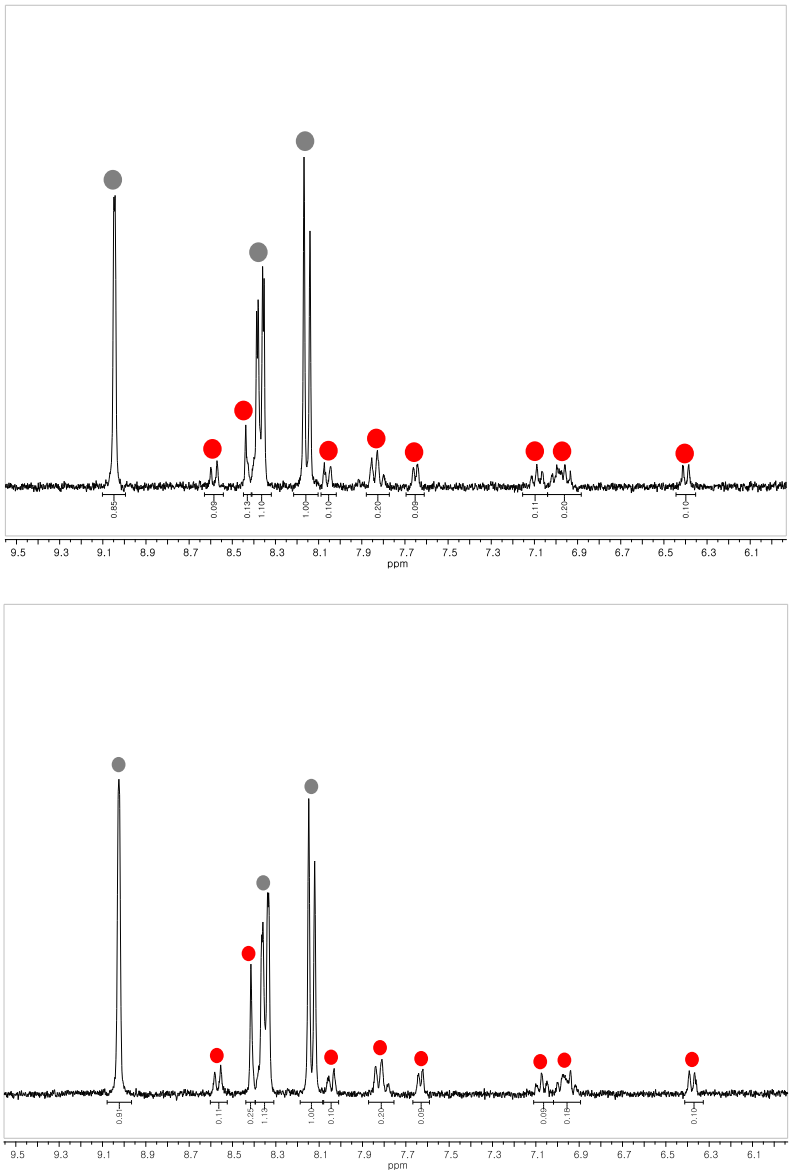

Figure 2.2 NMR digestion of Ir_BUiO in 0.3N NaOD D_2O solution (top). NMR digestion of $Pt_{0.1}$_Ir_BUiO in 0.3N NaOD D_2O solution (bottom). Hydrogen peaks of **L** (grey circle) and those of **Ir** (red circle).

H_2-Evolution Reaction

a. MOF system

Samples for photocatalytic hydrogen evolution with MOFs were prepared by sonicating the MOF samples (3.6 mg) in the solution of DMF:H_2O:DMA 8:2:2 v/v. The samples were stirred by magnetic stirring bar and gas in the samples were continuously exchanged with constant flow of Ar (5 sccm). Then, the samples were irradiated with 300 W Xe lamp equipped with an interference filter eliminating UV lights below 420 nm. The amounts of H_2 evolved within the samples were calculated each 30 min by TCD with the intergrated area of H_2 signal calibrated by the integrated area of Ar signal as an internal standard.

b. Homogeneous system

Samples for photocatalytic hydrogen evolution with homogeneous systems were prepared by dissolving Na^+**Ir**, H_2**Pt**, and H_2**L** in the solution of DMF:H_2O:DMA 8:2:2 v/v. The amounts of H_2 evolved within the samples were calculated according to the same method used in MOF system. In mercury poisoning test, sufficiently large amount of mercury (1.5 g) was added to the same solution and stirred severely with a magnetic stirring bar.

2.3 Result and discussion

As illustrated in Figure 2.3, Pt_n_Ir_BUiO comprises 2,2'-bipyridine-5,5'-dicarboxylate (**L**) as a self-healing site, Pt^{II}(**L**)Cl_2 (**Pt**) as a H_2-evolving catalyst, and $Ir^{III}(ppy)_2$(**L**) (**Ir**) as a photosensitizer (ppy is phenylpyridine). As controls, molecular catalyst, $Pt^{II}(H_2\mathbf{L})Cl_2$ (H_2**Pt**), and photosensitizer, $[Ir^{III}(ppy)_2(\mathbf{L})]^-Na^+$ (Na^+**Ir**), were separately synthesized according to the literature methods (H_2**L** is protonated **L**).[23,24] Three kinds of MOFs, $Pt_{0.8}$_Ir_BUiO, $Pt_{0.2}$_Ir_BUiO, and $Pt_{0.1}$_Ir_BUiO were synthesized by mixed-ligand synthesis with H_2**L** and Na^+**Ir** to yield Ir_BUiO, followed by post-synthetic metalation (PSM) with the varied feed amounts of Zeise's salt to graft Pt(II) (Figure 2.3). Powder x-ray diffraction (PXRD) patterns of the MOFs are in accordance with the simulated data from BUiO MOF single crystal (CCDC968930) and the MOFs are highly porous in terms of BET areas (Figure 2.4). Successful PSM was supported by Cl/Pt=2 ratio which is calculated from energy dispersive x-ray spectrometer (EDS) measurement (Figure 2.1 and Table 2.1). The ratio of each component in Pt_n_Ir_BUiO was determined by inductively coupled plasma-mass spectroscopy (ICP-MS) and ^{1}H NMR (the subscript n represents the ratio of **Pt** to **Ir**, see Supporting Information for detailed calculation). Field-emission scanning electron microscope (FE-SEM) shows that the size of MOF particles ranges from 100 to 300 nm (Figure 2.5).

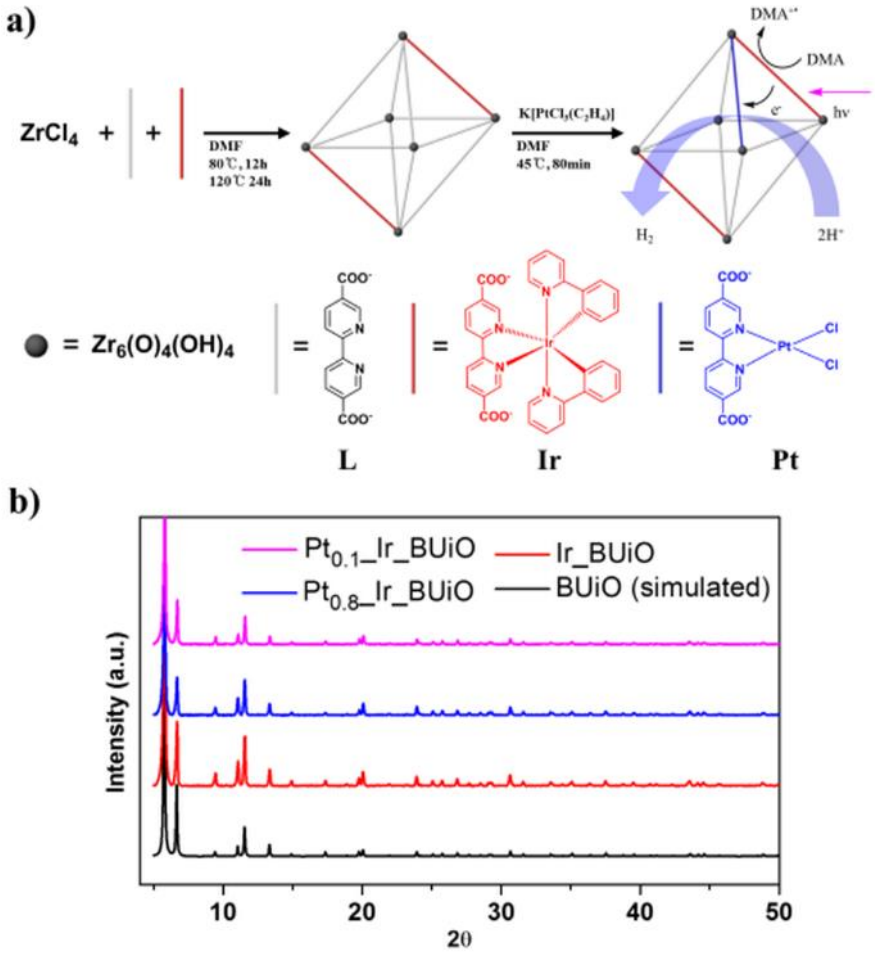

Figure 2.3 (a) The synthesis of Pt_n_Ir_BUiO and its operation. (b) PXRD pattern of $Pt_{0.1}$_Ir_BUiO (magenta), $Pt_{0.8}$_Ir_BUiO (blue), Ir_BUiO (red), and simulated BUiO (black).

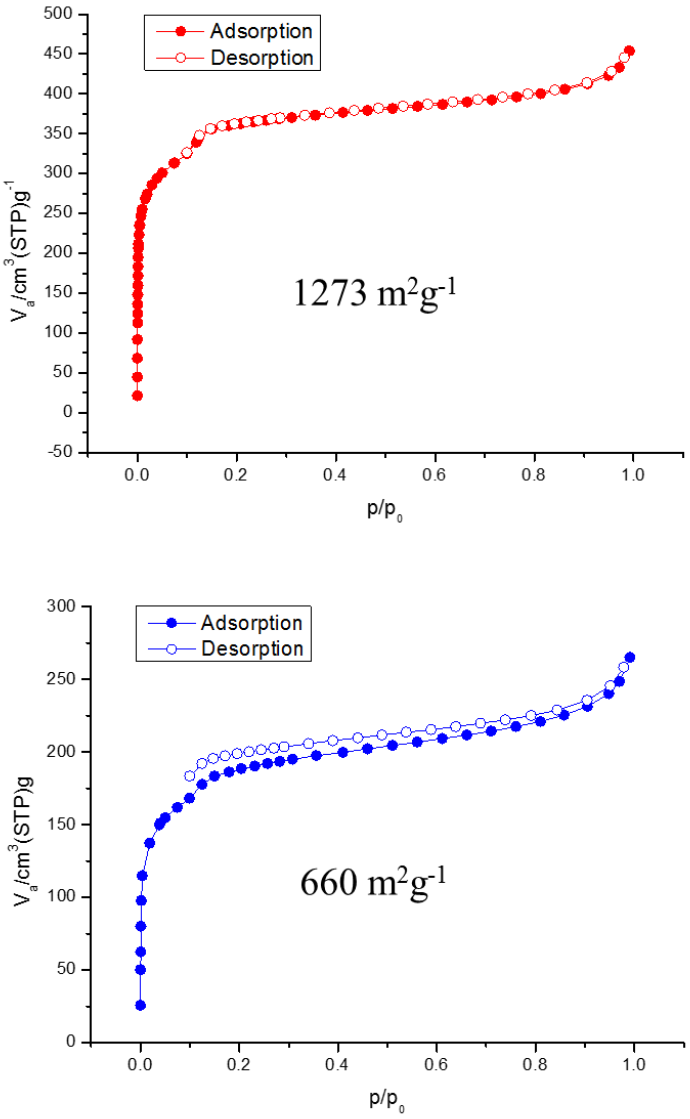

Figure 2.4 BET measurement of Ir_BUiO (left) and $Pt_{0.8}$_Ir_BUiO (right). The surface area of Ir_BUiO was comparable to those of analogous MOFs, Ru_UiO (1277 m^2g^{-1}) and Ir_UiO (1194 m^2g^{-1}).[17]

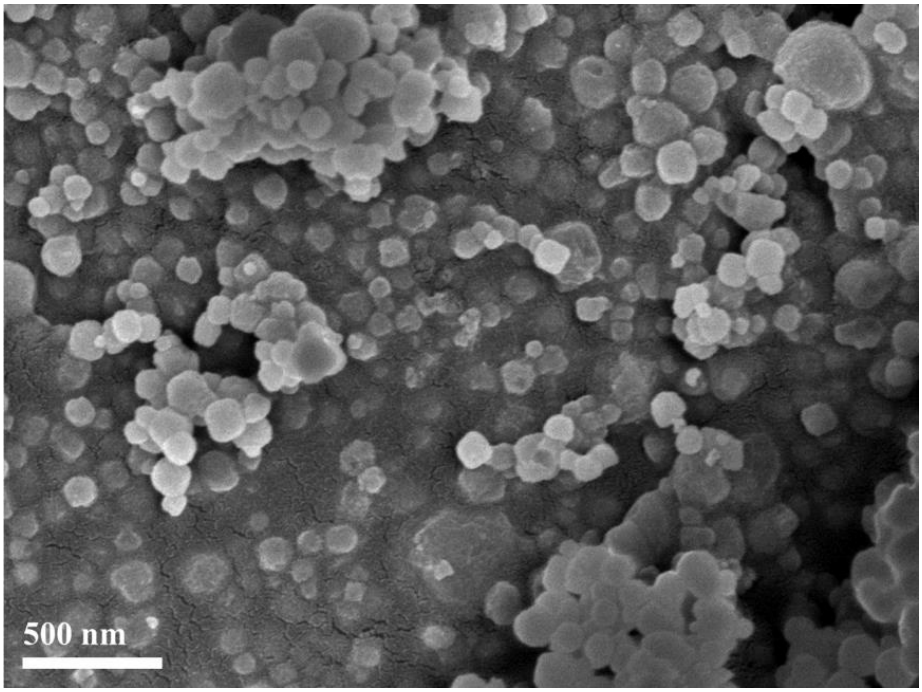

Figure 2.5 FE-SEM image of $Pt_{0.8}$_Ir_BUiO. The size of particles ranges from 100 nm to 300 nm.

To examine whether H_2**Pt** act as a molecular catalyst or just a precursor of Pt colloid, photocatalytic hydrogen evolution was carried out with H_2**Pt** and Na^+**Ir** in homogeneous system by irradiating visible light (see Supporting Information for experimental details). The kinetic curves for hydrogen production (Figure 2.6) show fast declining H_2-evolution rate and addition of mercury significantly attenuated the catalysis. As the process of colloidal formation is autocatalytic which quickly consumes all available molecular Pt(II) complex in the system, it can be concluded that active Pt colloid was formed as soon as the reaction started.[28] In accordance with the previous study, this result shows the weakness of H_2**Pt** under the photocatalytic condition to act as a precursor of Pt colloid.[8]

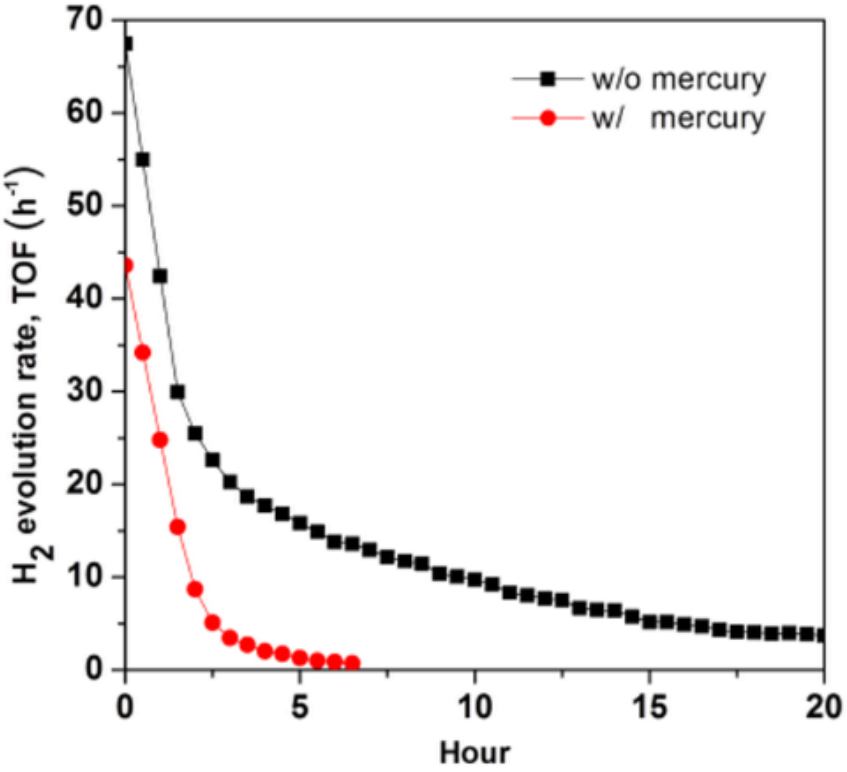

Figure 2.6 Photocatalytic hydrogen evolution with 0.55 μmol of Na^{+}**Ir** and 0.45 μmol of H_2**Pt** (black). The result of mercury poisoning experiment under the same conditions (red).

To prevent the colloidal formation by repairing H_2**Pt** in homogeneous system, 100 equiv. of excessive H_2**L** ligand with respect to H_2**Pt** was added according to the strategy of Eisenberg.[10,11] I envisaged that when Pt–diimine bond in H_2**Pt** is cleaved during hydrogen evolution, excessive H_2**L** ligand would promote re-coordination of Pt to its diimine sites and recover the molecular catalytic activity of H_2**Pt**. Upon photocatalysis, three different catalytic behaviors in terms of H_2-evolution rate were observed (Figure 2.7a). Mercury poisoning experiment confirms the molecular catalytic activity in the early stage (0–7.5 h) and subsequent colloidal Pt formation (7.5–9 h), followed by the catalytic activity of colloidal Pt after 9 h. The time period of molecular activity was prolonged as the ratio of H_2**L** to H_2**Pt** increased (Figure 2.7b and 2.8), implying that the abundancy of H_2**L** is important in extending the molecular catalytic activity. This result is consistent with the Eisenberg's experiment that showed increased amount of ligand molecule could further enhance such repair.[10] Finally, to test the importance of diimine sites, 13 equiv. of biphenyl-4,4'-dicarboxylic acid was added as a control instead of H_2**L**. Only the colloidal activity was observed in this case without any repair of the catalyst (Figure 2.9).

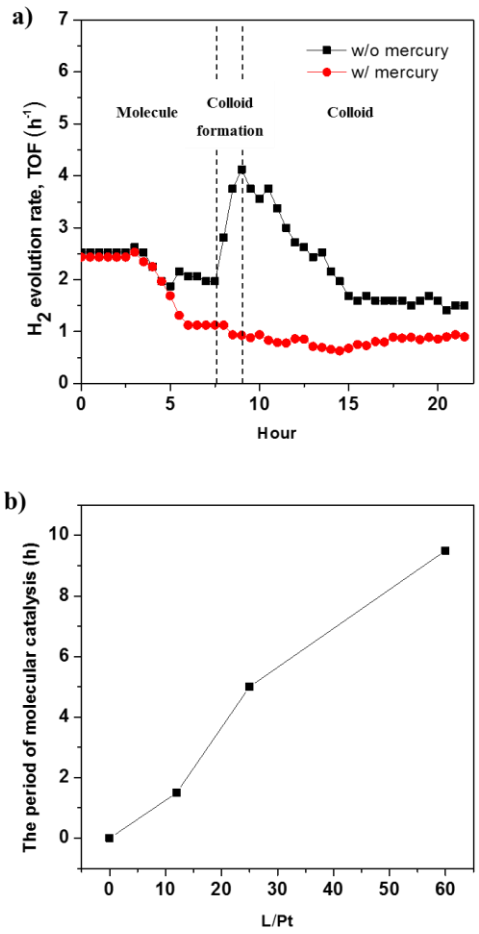

Figure 2.7 (a) Photocatalysis driven with 0.30 μmol of Na^{+}**Ir**, 0.029 μmol of H_2**Pt**, and 3.0 μmol of H_2**L** (black). The result of mercury poisoning experiment under the same conditions (red). (b) The period of molecular catalysis with 0, 13, 25, and 60 equiv. of H_2**L** per H_2**Pt** (with 0.55 μmol of Na^{+}**Ir** and 0.45 μmol of H_2**Pt**). Each recorded TON of 0, 2.52, 10.7, and 18.4, respectively.

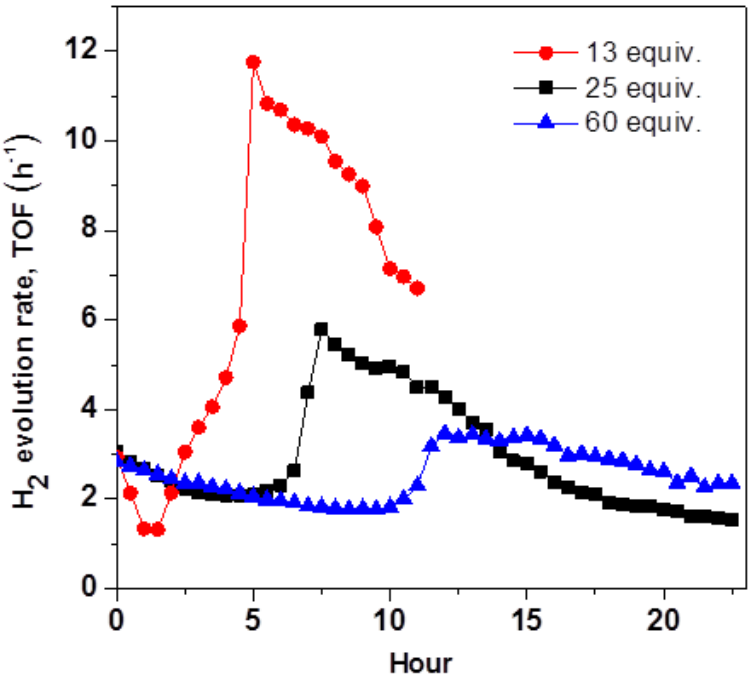

Figure 2.8 H_2-evolution reaction with 0.55 μmol of Na^+**Ir**, 0.45 μmol of H_2**Pt**, and 13 equiv. (red), 25 equiv. (black), and 60 equiv. (blue) of H_2**L** per H_2**Pt**.

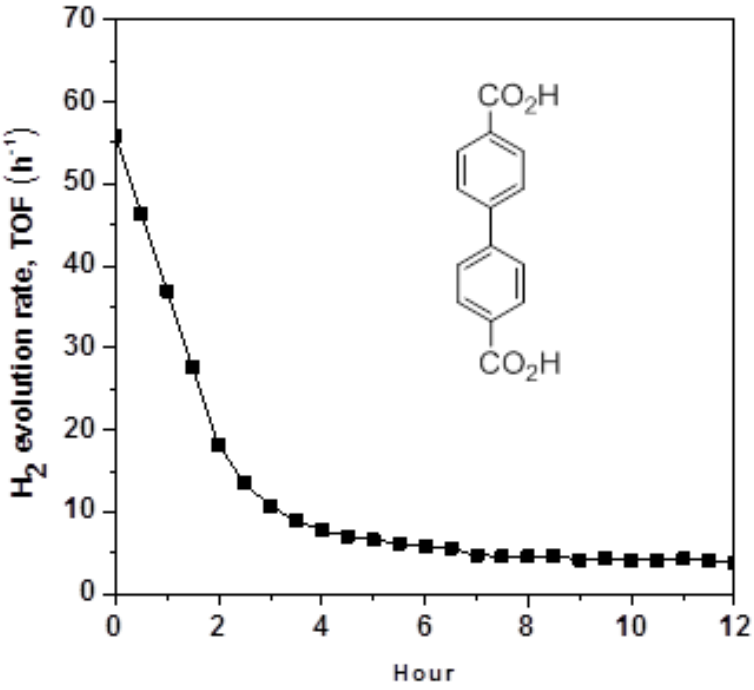

Figure 2.9 The repairing effect does not occur when biphenyl-4,4'-dicarboxylic acid is added.

The photocatalytic experiment with $Pt_{0.1}$_Ir_BUiO was conducted with same conditions described above. $Pt_{0.1}$_Ir_BUiO has **L** to **Pt** ratio of 100 measured by ^{1}H-NMR and ICP-MS. Stable molecular catalytic activity was observed recording 343 $TON_{6.5days}$ and 2.9 h^{-1} TOF_{max}, the highest TON among the systems using molecular Pt(II) catalysts (Figure 2.10 and 11).[2,4,20,22] The high resolution transmission electron microscope (HR-TEM) image confirms no trace of Pt colloid inside the $Pt_{0.1}$_Ir_BUiO even after 6.5 days of photocatalytic hydrogen evolution (inset of Figure 2.10). The initial period in which the H_2-evolution rate gradually increases is, thus, due to the induction period required for the system to reach the steady state, not due to colloidal Pt formation.[29,30] It is noteworthy that the molecular catalytic activity of $Pt_{0.1}$_Ir_BUiO lasted more than 6.5 days, while that of the control homogeneous system with same amount of each species ceased in 7.5 h (Table 2.2). Such an outstanding performance of MOF system suggests that not only the abundancy of free ligand, but the proximity between the catalyst and free ligand plays a crucial role in self-healing.

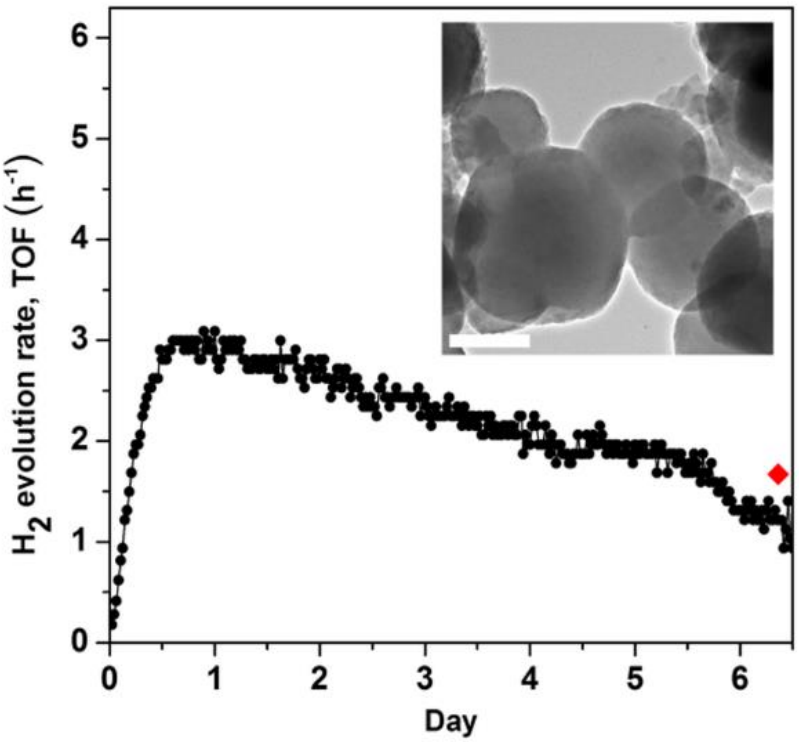

Figure 2.10 H_2-evolution rate of $Pt_{0.1}$_Ir_BUiO. The MOF contains 0.30 μmol of **Ir**, 0.029 μmol of **Pt**, and 3.0 μmol of **L**. Inset: HR-TEM image of $Pt_{0.1}$_Ir_BUiO after 6.5 days of photocatalytic hydrogen evolution (red square). Bar represents 200 nm.

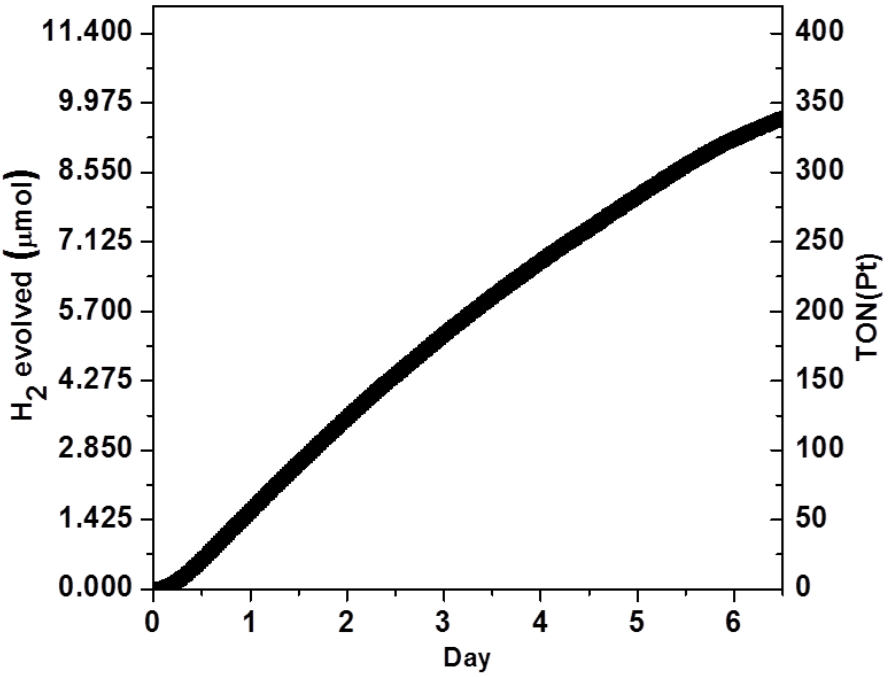

Figure 2.11 H_2-evolution of $Pt_{0.1}$_Ir_BUiO and the TON of **Pt**, TON = n(H_2)/n(**Pt**). The MOF contains 0.30 μmol of **Ir**, 0.029 μmol of **Pt**, and 3.0 μmol of **L**.

Table 2.2 Comparison between MOF systems ($Pt_{0.8}$_Ir_BUiO, $Pt_{0.2}$_Ir_BUiO, $Pt_{0.1}$_Ir_BUiO) and homogeneous counterparts.

Entry	The ratio of **L** to **Pt**[a]	Molecular catalytic activity	Colloidal formation	Colloidal catalytic acitvity	TON[b]
MOF	12.5 ($Pt_{0.8}$)	**0−24 h**	24−40 h	after 40 h	79.8
	62.5 ($Pt_{0.2}$)	**0−38 h**	38−50 h	after 50 h	114
	100 ($Pt_{0.1}$)	**≥160 h**	-	-	343
Homogeneous	12.5	**0−1.5 h**	1.5 h−5 h	after 5 h	2.52
	100	**0−7.5 h**	7.5 h−9 h	after 9 h	16.9

a. The ratio of H_2**L** to H_2**Pt** for homogeneous system.

b. TON of molecular Pt(II) catalyst after molecular photocatalysis.

The MOFs with varied **L** to **Pt** ratios were subject to photocatalytic hydrogen evolution and their influence on colloidal formation was investigated. Compared to the **L** to **Pt** ratio in $Pt_{0.1}$_Ir_BUiO, $Pt_{0.2}$_Ir_BUiO and $Pt_{0.8}$_Ir_BUiO have smaller **L** to **Pt** ratio of 62.5 and 12.5, respectively. $Pt_{0.8}$_Ir_BUiO showed molecular catalytic activity at the initial stage (0–1 day) and sequent colloidal formation (1–1.7 days), followed by the catalytic activity of colloidal Pt after 1.7 days (Figure 2.12a). HR-TEM study confirms these results that there was no colloidal Pt in the early stage (1 day, Figure 2.12b), which contrasts with the observation of several nano-sized Pt colloids after 5 days (Figure 2.12c). Such transformation of molecular catalytic activity into colloidal catalytic activity correlates well with the homogeneous system in which decreased **L** to **Pt** ratio resulted in the faster colloidal formation, *vide supra*. In addition, photocatalytic hydrogen evolution with $Pt_{0.2}$_Ir_BUiO showed intermediate self-healing period of 38 h, which also follows this trend (Figure 2.13). These results indicate that the MOF systems are superior in self-healing compared to the homogeneous counterparts (Table 2.2) and the complete inhibition of colloidal formation can be established when sufficiently large **L** to **Pt** ratio is guaranteed in MOF system.

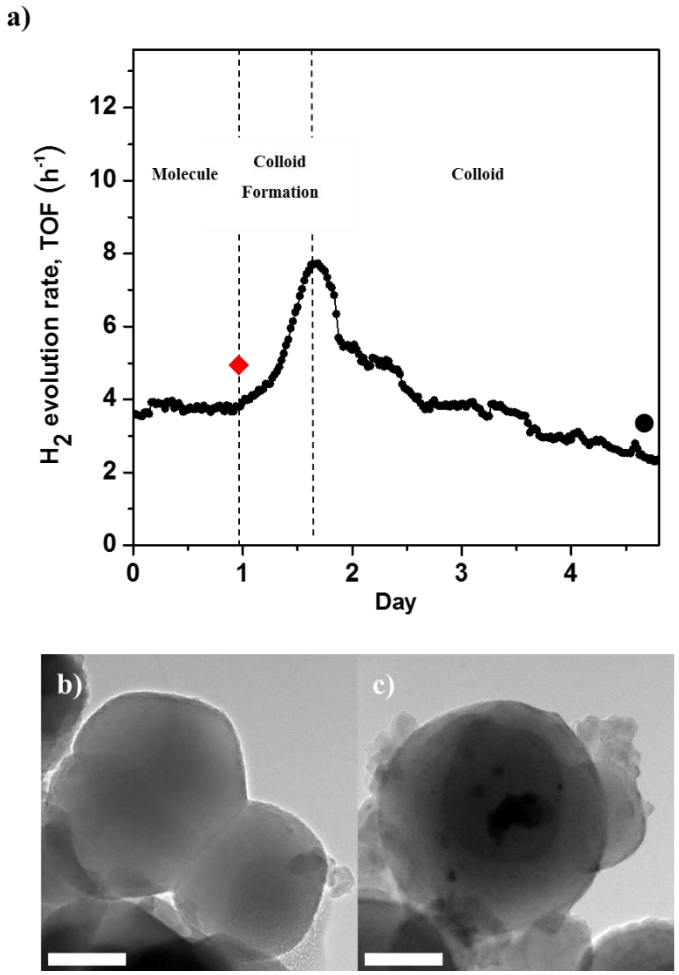

Figure 2.12 (a) H_2-evolution rate of $Pt_{0.8}$_Ir_BUiO with three different catalytic regions, photocatalysis driven by molecular (first region), molecular + colloidal (second region), and colloidal (third region) catalyst. (b) HR-TEM image of $Pt_{0.8}$_Ir_BUiO after 1 day of photocatalytic hydrogen evolution, red square in (a). (c) HR-TEM image after 5 days, black circle in (a). Bar in (b) and (c) represents 200 nm.

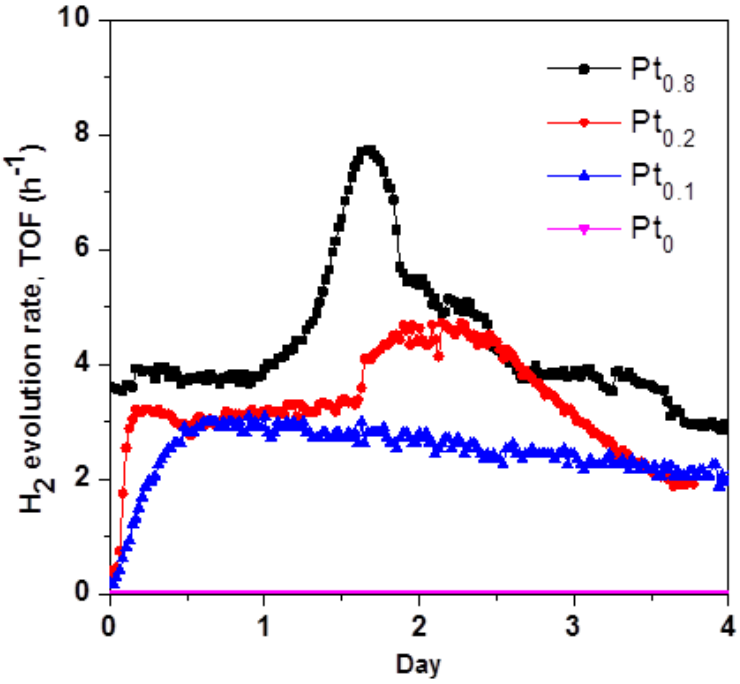

Figure 2.13 H_2-evolution rate of each MOF with the varied amount of **Pt**, $Pt_{0.8}$_Ir_BUiO (black), $Pt_{0.2}$_Ir_BUiO (red), $Pt_{0.1}$_Ir_BUiO (blue), and Ir_BUiO (magenta).

Importantly, as can be seen in Table 2.2, three MOFs showed high robustness during molecular photocatalysis. For them to achieve such a superior stability, I thought that self-healing of iridium photosensitizer might have also occurred. To examine the self-healing of **Ir**, I conducted degradation experiment with Na^+**Ir** in two batches of solution (DMF/H_2O/DMA = 8/2/2), with and without 12 equiv. of H_2**L**. Irradiation of visible light with 420 nm cut-off filter resulted in decreased absorbance of Na^+**Ir** in both batches, but each showed difference after 2 h. Figure 2.14 shows that absorbance of Na^+**Ir** in a batch without H_2**L** kept decreasing until 7 h, and that of MLCT region became very weak. However, in another batch with 12 equiv. of H_2**L**, absorbance reached equilibrium after 2 h of irradiation and there was no more deactivation. This result explains that the healing of Na^+**Ir** by H_2**L** may also work, and stable catalytic activity in MOF system can be attributed to the efficient self-healing of both **Pt** and **Ir**. Also, the leaching amounts of **Pt** and **Ir** after 24 h of photocatalysis with $Pt_{0.8}$_Ir_BUiO was calculated from ICP-MS and the amounts were only 1.7% and 3.9%, respectively, confirming that the photocatalysis was driven inside the MOF by molecular catalyst and photosensitizer.

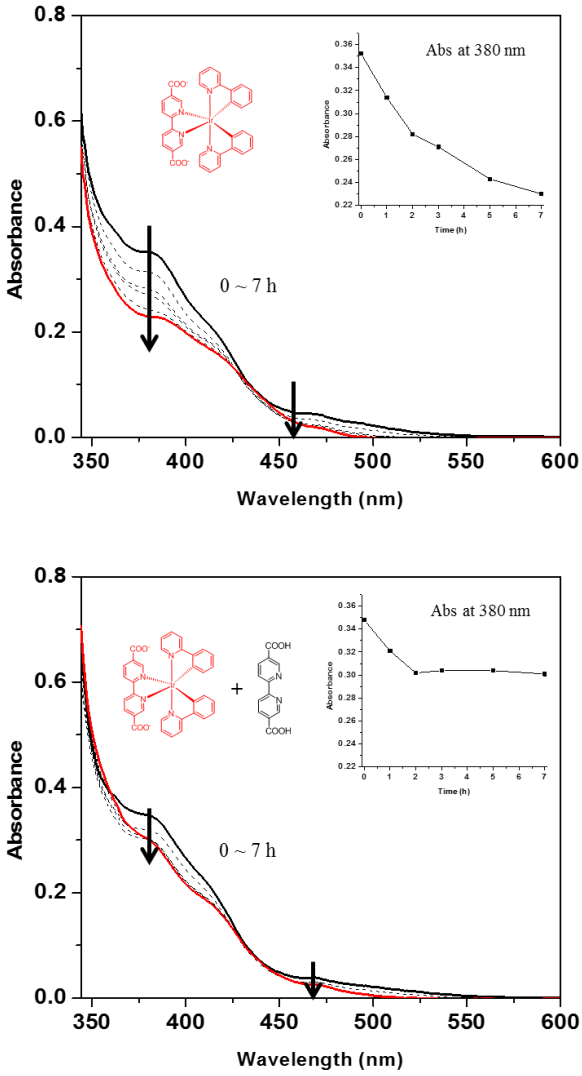

Figure 2.14 Photodegradation experiement with 500 µM Na^{+}**Ir** in the solution of DMF:H_2O:DMA 8:2:2 v/v. Without 12 equiv. H_2**L** (top) and with 12 equiv. H_2**L** (bottom, the absorbance of H_2**L** was subtracted).

2.4 Conclusions

In conclusion, the integration of **Pt**, **Ir**, and excessive amount of **L** into UiO-67 MOF enabled self-healing of **Pt** during photocatalytic hydrogen evolution. The observed TON of molecular Pt(II) catalyst on MOF in this work is the highest among molecular Pt(II) catalysts ever reported. I have successively demonstrated the principle of self-healing, its dependence on the ratio of **L** to **Pt**, and the superiority of MOF system as a self-healing platform. In addition, long lasted debate on the fate of Pt(II) catalysts during photocatalysis (molecular or colloidal) was resolved in this work by clarifying the evolution of molecular Pt(II) catalyst to the colloidal Pt catalyst.[2,6,8] Since many transition metal complexes are widely used in various photocatalysis, I believe that this novel strategy would pave a way towards highly stable photocatalytic system.

2.5 References

1. Umena, Y.; Kawakami, K.; Shen, J. R.; Kamiya, N. *Nature* **2011**, *473*, 55.
2. Ozawa, H.; Sakai, K. *Chem. Commun.* **2011**, *47*, 2227.
3. Stoll, T.; Gennari, M.; Fortage, J.; Castillo, C. E.; Rebarz, M.; Sliwa, M.; Poizat, O.; Odobel, F.; Deronzier, A.; Collomb, M. N. *Angew. Chem. Int. Ed.* **2014**, *53*, 1680.
4. Knoll, J. D.; Arachchige, S. M.; Brewer, K. J. *ChemSusChem* **2011**, *4*, 252.
5. Artero, V.; Fontecave, M. *Chem. Soc. Rev.* **2013**, *42*, 2338.
6. Eckenhoff, W. T.; Eisenberg, R. *Dalton Trans.* **2012**, *41*, 13004.
7. Pfeffer, M. G.; Schafer, B.; Smolentsev, G.; Uhlig, J.; Nazarenko, E.; Guthmuller, J.; Kuhnt, C.; Wachtler, M.; Dietzek, B.; Sundstrom, V.; Rau, S. *Angew. Chem. Int. Ed.* **2015**, *54*, 5044.
8. Du, P.; Schneider, J.; Li, F.; Zhao, W.; Patel, U.; Castellano, F. N.; Eisenberg, R. *J. Am. Chem. Soc.* **2008**, *130*, 5056.
9. Lutterman, D. A.; Surendranath, Y.; Nocera, D. G. *J. Am. Chem. Soc.* **2009**, *131*, 3838.
10. Lazarides, T.; McCormick, T.; Du, P. W.; Luo, G. G.; Lindley, B.; Eisenberg, R. *J. Am. Chem. Soc.* **2009**, *131*, 9192.
11. McCormick, T. M.; Han, Z.; Weinberg, D. J.; Brennessel, W. W.; Holland, P. L.; Eisenberg, R. *Inorg. Chem.* **2011**, *50*, 10660.

12. Manna, K.; Zhang, T.; Lin, W. *J. Am. Chem. Soc.* **2014**, *136*, 6566.
13. Manna, K.; Zhang, T.; Greene, F. X.; Lin, W. *J. Am. Chem. Soc.* **2015**, *137*, 2665.
14. Falkowski, J. M.; Sawano, T.; Zhang, T.; Tsun, G.; Chen, Y.; Lockard, J. V.; Lin, W. *J. Am. Chem. Soc.* **2014**, *136*, 5213.
15. Fei, H.; Cohen, S. M. *J. Am. Chem. Soc.* **2015**, *137*, 2191.
16. Fei, H.; Shin, J.; Meng, Y. S.; Adelhardt, M.; Sutter, J.; Meyer, K.; Cohen, S. M. *J. Am. Chem. Soc.* **2014**, *136*, 4965.
17. Wang, C.; deKrafft, K. E.; Lin, W. *J. Am. Chem. Soc.* **2012**, *134*, 7211.
18. Zhang, Z. M.; Zhang, T.; Wang, C.; Lin, Z.; Long, S.; Lin, W. *J. Am. Chem. Soc.* **2015**, *137*, 3197.
19. Maza, W. A.; Padilla, R.; Morris, A. J. *J. Am. Chem. Soc.* **2015**, *137*, 8161.
20. Hou, C.-C.; Li, T.-T.; Cao, S.; Chen, Y.; Fu, W.-F. *J. Mater. Chem. A* **2015**, *3*, 10386.
21. Pullen, S.; Fei, H.; Orthaber, A.; Cohen, S. M.; Ott, S. *J. Am. Chem. Soc.* **2013**, *135*, 16997.
22. Zhou, T.; Du, Y.; Borgna, A.; Hong, J.; Wang, Y.; Han, J.; Zhang, W.; Xu, R. *Energy Environ. Sci.* **2013**, *6*, 3229.
23. Tamayo, A. B.; Alleyne, B. D.; Djurovich, P. I.; Lamansky, S.; Tsyba, I.; Ho, N. N.; Bau, R.; Thompson, M. E. *J. Am. Chem. Soc.* **2003**, *125*, 7377.
24. Szeto, K. C.; Kongshaug, K. O.; Jakobsen, S.; Tilset, M.; Lillerud, K. P. *Dalton Trans.* **2008**, *15*, 2054.
25. Kandiah, M.; Nilsen, M. H.; Usseglio, S.; Jakobsen, S.; Olsbye, U.;

Tilset, M.; Larabi, C.; Quadrelli, E. A.; Bonino, F.; Lillerud, K. P. *Chem. Mater.* **2010**, *22*, 6632.

26. Sánchez-Sánchez, M.; Getachew, N.; Díaz, K.; Díaz-García, M.; Chebude, Y.; Díaz, I. *Green Chem.* **2014**, *17*, 1500.
27. DeCoste, J. B.; Peterson, G. W.; Jasuja, H.; Glover, T. G.; Huang, Y.-g.; Walton, K. S. *J. Mater. Chem. A* **2013**, *1*, 5642.
28. Besson, C.; Finney, E. E.; Finke, R. G. *J. Am. Chem. Soc.* **2005**, *127*, 8179.
29. This phenomenon is probable in that charged species in MOF can enhance the interaction between MOF and H_2, and UiO MOF can store small amount of hydrogen in room temperature. Such a trapping effect might obstruct H_2 escaping from MOFs and it seems to become more influential when the absolute H_2-evolution rate is decreased because UiO MOF can store small amount of H_2.The facts that the induction period of $Pt_{0.2}$_Ir_BUiO is shorter than $Pt_{0.1}$_Ir_BUiO and is followed by colloidal formation both support my explanation (Figure 2.13). In addition, the HR-TEM image in Figure 3 showed no Pt colloid.
30. Vasanth Kumar, K.; Charalambopoulou, G.; Kainourgiakis, M.; Stubos, A.; Steriotis, T. *Comput. Theor. Chem.* **2015**, *1061*, 36.

Chapter 3. Self-Assembly of Octahedral Iridium(III) Photosensitizer for Photocatalytic Hydrogen Evolution from Water

3.1 Introduction

As a prototype of light-harvesting complexes in nature, chloroplast in green plants transforms solar energy into chemical fuels through photosynthesis. In chloroplast, PSI and PSII are the key proteins for solar-to-fuel conversion, containing catalytic metal clusters surrounded by light-harvesting antenna.[1] These photosynthetic systems are constructed through self-assembly, and their sophisticated structure enables efficient charge transfer during photosynthesis.[2] To mimic natural photosynthesis and realize highly efficient solar-to-fuel conversion, there have been various efforts to exploit supramolecular assembly of organic molecules to build integrated photocatalytic systems in water. Such supramolecular platforms could incorporate both photosensitizer and catalyst, and the resulting integrated systems showed enhanced photocatalytic activity in water splitting or visible-light-driven NADH regeneration.[1, 3-5]

Octahedral Ir(III) complexes have been widely used as photosensitizer for photocatalytic hydrogen evolution due to their high visible light absorption,

long lifetime, and high thermal stability. Despite their outstanding properties, their molecular recognition capability has not been explored intensively so far. This is because the octahedral structure of Ir(III) photosensitizers, which seemingly lacks self-assembly motif, has hampered their supramolecular approach. While there was a report on octahedral Ir(III) complexes which can form hydrogels through self-assembly, the mechanism has not been clarified yet.[6]

Herein, I report an amphiphilic Ir(III) complex, namely **Ir**, which can self-assemble in water and also propose its self-assembly mechanism. The self-assembly was proposed to occur via hydrophobic collapse which promotes one-to-one interaction of **Ir**'s two stereoisomers, and was examined with ^{1}H NMR. Interestingly, when sodium chloride salt was added to induce the charge screening effect, electrostatic repulsion between self-assembled structures became weaker and the solution became a hydrogel. Also, this hydrogel showed far enhanced quantum yield than the solution state by circumventing **Ir**'s non-radiative decay. Using **Ir** as a supramolecular platform, I could make an integrated hydrogel system comprised of **Ir** as a photosensitizer, Pt colloid as a catalyst, TEOA as a sacrificial reducing agent, and water as a proton source. Under visible-light irradiation, the system produced about ten-times more amount of hydrogen than its control system, and thus showed the superiority of integrated systems in photocatalytic reactions.

3.2 Experimental section

General Methods

Commercially available chemicals were purchased from Sigma-Aldrich, Acros, and Alfa Aesar, unless otherwise noted, and used as received. All glasswares and magnetic stirring bars were thoroughly dried in an oven (60 ℃). Reactions were monitored using thin layer chromatography (TLC). Commercial TLC plates (silica gel 254, Merck Co.) were developed and the spots were visualized under UV light at 254 or 365 nm. Silica gel column chromatography was performed with silica gel 60G (particle size 5-40 μm, Merck Co.). ^{1}H NMR spectra were collected with a Bruker AVANCE-300 NMR spectrometer. Chemical shifts (δ) are given in ppm and referenced to TMS. Field emission scanning electron microscope (FE-SEM) images and energy-dispersive x-ray spectroscopy (EDS) data were acquired on a JEOL, JSM-6700F microscope.

Synthesis of $[Ir(ppy)_2(L)]^-Na^+ \cdot 1.5H_2O$ (Ir)

$[Ir(ppy)_2(\mu\text{-}Cl)]_2$ was synthesized according to the literature procedure.[8] $[Ir(ppy)_2(\mu\text{-}Cl)]_2$ (500 mg) and 2,2'-bipyridine-5,5'-dicarboxylic acid (274 mg) were dispersed in 50 ml ethylene glycol. The mixture was stirred at 150 ℃ for 4 h under Ar atmosphere. The crude product was cooled to room temperature

and put dropwise into water. Resulting suspension was washed with water, filtered, and dried overnight in vacuum oven at 60 ℃. Dried solid was dispersed in methanol and droplets of 0.3N NaOH were added until the solution becomes clear. The resulting solution was evaporated and purified using a silica gel column chromatography with MeOH and the mixed solution of MeOH:MC 1:1 v/v as eluents, followed by reprecipitation in acetone.

Red solid, Yield: 402 mg (52 %). ^{1}H NMR (300 MHz, D_2O) δ 8.61 (d, J = 8.4 Hz, 2H), 8.45 (dd, J = 8.4, 2.1 Hz, 2H), 8.42 (s, 2H), 8.10 (d, J = 8.0 Hz, 2H), 7.92 – 7.81 (m, J = 14.9, 7.9 Hz, 4H), 7.70 (d, J = 5.3 Hz, 2H), 7.12 (t, J = 7.1 Hz, 2H), 7.02 (t, 2H), 6.98 (t, 2H), 6.44 (d, J = 7.4 Hz, 2H). Anal. Calcd for $C_{34}H_{25}IrN_4NaO_{5.5}$: C, 51.5%; H, 3.18%; N, 7.07%, Found: C, 51.7%; H, 3.16%; N, 6.88%. Energy-dispersive x-ray spectroscopy (EDS) measurement of the Ir complex showed Na/Ir ratio of 1.05.

TEM analysis

To see the nanostructure of **Ir** in water, I dropped a droplet of **Ir** solutions on a TEM grid at various concentrations and left to evaporate. At the high concentrations, however, only aggregated particles of **Ir** were observed because **Ir** aggregated each other during the evaporation of water. When I lowered the concentration to 1.0 mM, I could finally see the needle-like structure of **Ir** (Figure 3.5), which is formed by self-assembly as water evaporated.

Photocatalytic H_2-Evolution Reaction

The samples were put into 20 ml vial and irradiated with 300 W Xe lamp equipped with an interference filter eliminating UV lights below 420 nm. The amounts of H_2 evolved within the samples were calculated each 30 min by TCD with the intergrated area of H_2 signal calibrated by the integrated area of Ar signal as an internal standard.

- WS sol

To make a aqueous solution which contains TEOA as a sacrificial reducing agent, I mixed 1.8 ml of H_2O with 200 µl of TEOA, followed by neutralization with 200 µl of 1N HCl solution.

- Gel vs Sol

To make a gel attached on a glass, 1.5 cm x 1.5 cm square glass was prepared and layed on the bottom of the 20 ml vial. Note that weight of the glass and the vial were measured in advance. Then, 8.3 mg of K_2PtCl_4 was dissolved in 20 ml H_2O and 1.8 ml of this solution was mixed with 200 µl of TEOA, followed by neutralization with 200 µl of 1N HCl solution. This solution, namely 'WS sol with Pt', was then poured into the 20 ml vial and 30 mg of **Ir** was dissolved in this solution with enough heat. After a few minutes of cooling, **Ir** gel was formed on the square glass and I took the glass out of the 20 ml vial. The amount of the gel attached on the glass was measured by weighing them together at first, then subtracting weight of the glass from the

total weight. It was calculated that 0.2 ml WS sol, 7.9 µmol **Ir**, and 0.16 µmol K_2PtCl_4 were in the gel. I standed it in water splitting cell to be fully irradiated by Xenon lamp and started photocatalysis (Figure 3.8).

I prepared a rectangular cuvette and 'WS sol with Pt' was poured into it until the height of the solution reached to 2.25 cm which amounts to the same irradiation area with the glass, mentioned above, when multiplied with the width (1.0 cm) of the cuvette (I modulated the amount of K_2PtCl_4 dissolved in WS sol to be commensurate with the above gel system). Then, I put same amount of **Ir** into WS sol and this solution became sol due to low concentration.

- Ir vs protonated **Ir**

When 1N HCl was added dropwise to **Ir** aqeous solution, the formation of precipitate can be observed as **Ir** became protonated. I compared photocatalytic activity of this protonated **Ir** and **Ir** (2.5 mM) by using Pt colloid (2.5 mM) as a catalyst.

3.3 Result and discussion

A previous research done by Yogesh et al. discovered cationic iridium complexes that can self-assemble in water and form hydrogel with their carboxylate counteranions.[6] X-ray analysis revealed that the gelation occurs with the close packing of the supramolecular columns sheathed in their solvation shell into a 2D rectangular shape (Figure 3.1). However, its mechanism on how they interact each other to make rectangular column was still remained elusive.

To reveal the mechanism of self-assembly and use it for further applications, I synthesized an amphiphilic iridium complex by functionalizing iridium metal center with phenylpyridine as hydrophobic ligands and 2,2'-bipyridine-5,5'-dicarboxylate as a hydrophilic ligand, namely **Ir** (Figure 3.2). Integration of carboxylate anion into iridium complex enables further application of this iridium hydrogel for multi-component system, such as water-splitting, without the operation of their counteranions. I then investigated the formation of hydrogel via self-assembly by dissolving 3 wt% **Ir** into DI water. However, this **Ir** aqueous solution only became viscous liquid and the viscosity was too low to form hydrogel. I assumed that the electrostatic repulsion between each anionic **Ir** column hampered their interaction to form hydrogel. To eliminate like-charge repulsion, I increased the ionic strength of the solution by adding enough amount of sodium chloride and the principle is described in Scheme 3.1. As a result, NaCl actually worked as a charge screening agent in

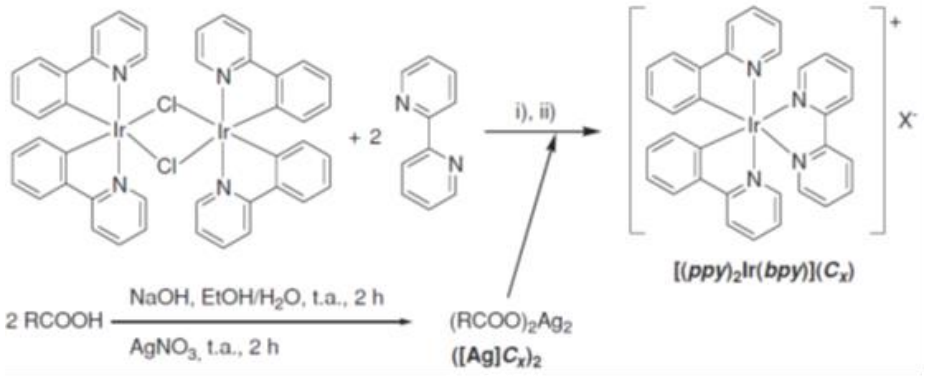

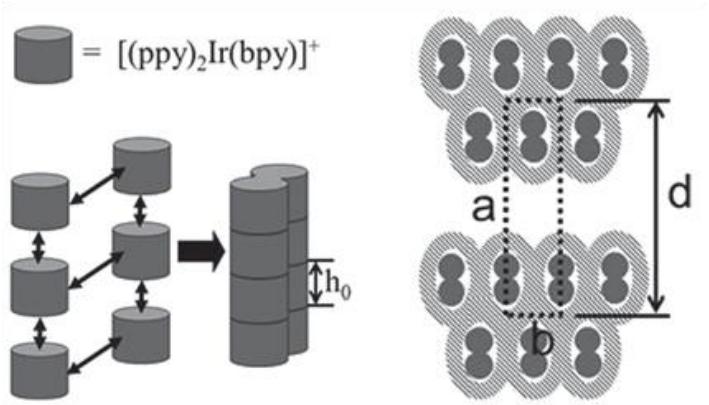

Figure 3.1 The synthesis of the reported Ir(III) complexes which can self-assemble in water and their nanostructures revealed by X-ray analysis.[6]

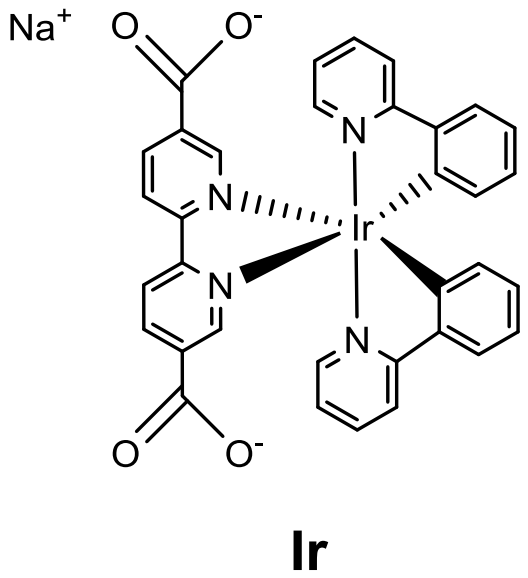

Figure 3.2 The structure of **Ir**, $[Ir(ppy)(dcbpy)]^{-}\cdot Na^{+}$ (ppy is phenylpyridine and dcbpy is 2,2'-bipyridine-5,5'-dicarboxylate).

solution and decreased the debye length of anionic Ir columns.[7] Interestingly, even with 0.5 wt% of iridium complex, NaCl-added solution became a hydrogel as can be evaluated by 'stable to inversion of test tube' method (Figure 3.3). Next, for further application in photocatalytic water reduction, I tested gelation with TEOA solution neutralized with 5N HCl (WS sol) and it also acted as a charge screening agent as TEOA dissolves into ions in water.

Transmission electron microscopy (TEM) of dried **Ir** solution in Figure 3.4 revealed very thin needle-like structure which may form supramolecular fiber in gel state (see experimental details in Experimental section). It is assumed that this needle structure might be originated from the lamello-collumnar structure, the substructure of which is formed by the lateral interaction of **Ir** columns.[6] In addition, the mechanism on how these **Ir** columns are made from the self-assembly of **Ir** can be explained by hydrophobic collapse of phenylpyridine ligands. It is well-known that the iridium complexes synthesized through Nonoyama reaction consist of two stereoisomers in equal amount, called Δ and Λ.[9] Thus, one-to-one hydrophobic interaction between the phenylpyridine ligands of two stereoisomers may drive self-assembly in the way depicted in Scheme 3.2. This mechanism is supported by NMR analysis with increasing the concentration of **Ir** in deuterated water. As can be seen in Figure 3.5a, hydrogen peaks assigned to phenylpyridine ligand shift up-field with increasing concentration of **Ir**, while those of 2,2'-bipyridine-5,5'-dicarboxylate rarely do. This means that phenylpyridine ligand interacts one another with the increasing concentration of **Ir**, as depicted in Scheme 3.2, while 2,2'-bipyridine-5,5'-dicarboxylate does not.

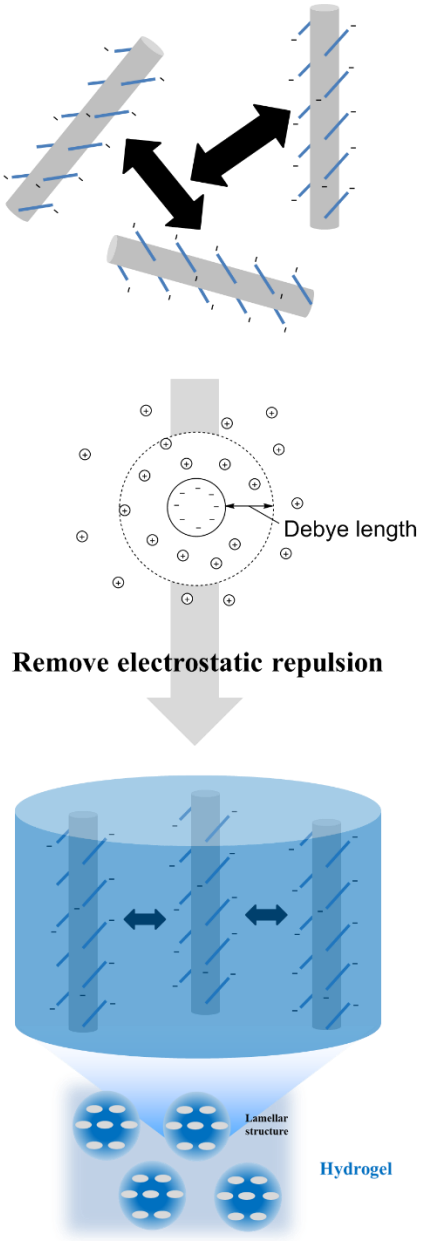

Scheme 3.1 The effect of NaCl as a charge screening agent and the formation of self-assembled **Ir** columns in NaCl solution.

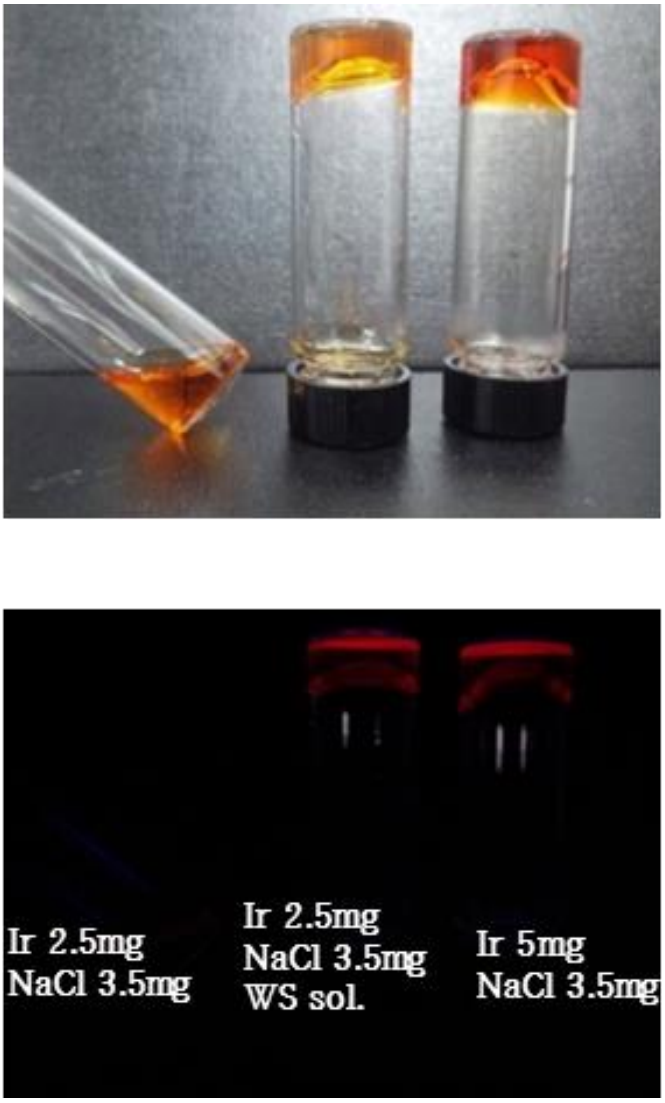

Figure 3.3 The gelation was confirmed by stable-to-inversion method and it showed red photoluminescence under 365 nm irradiation.

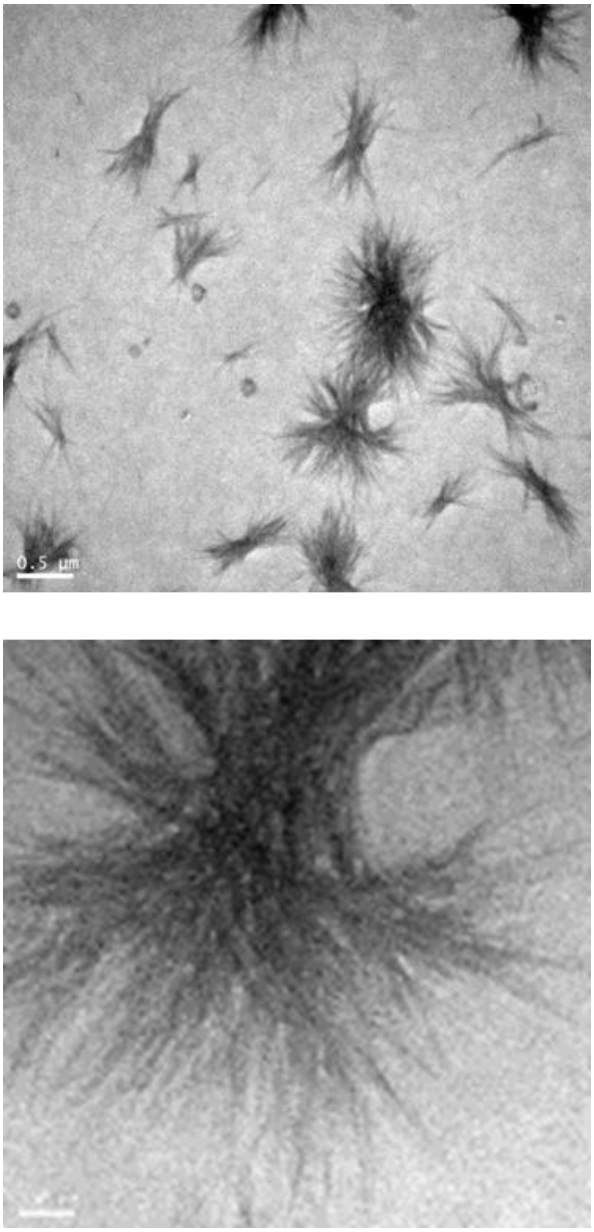

Figure 3.4 Niddle-like structure of dried **Ir** solution. Bar represents 0.5 µm (top) and 100 nm (bottom).

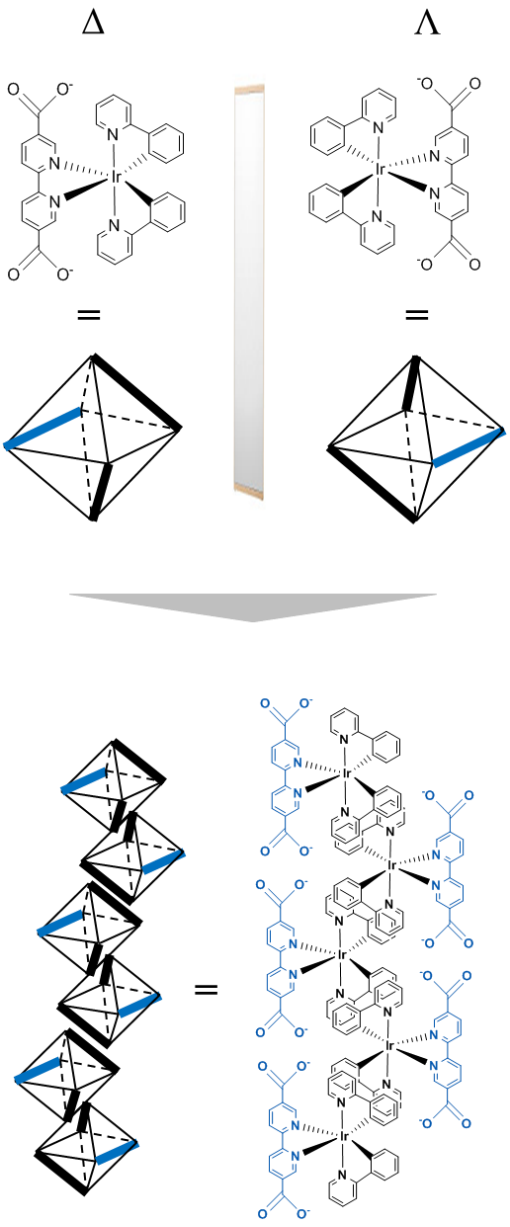

Scheme 3.2 One-to-one interaction between the phenylpyridine ligands in two stereoisomers, which induces self-assembly of **Ir** column.

When I increase the amount of NaCl in 2.5 mM Ir solution, however, such up-field shift was not observed and it can be concluded that NaCl just act as without inducing any hydrophobic collapse (Figure 3.5b).

To examine the dependency of self-assembly on concentration and temperature, I investigated the change in UV/Vis absorption spectra by increasing the concentration of **Ir** and its temperature. Self-assembly can be rationalized if critical gelation concentration and temperature are observed with similar spectral shifts in both cases. As can be seen in Figure 3.6a, abrupt bathochromic shift of ^{1}LLCT and increase in the absorption of ^{1}MLCT and ^{3}MLCT can be observed when the concentration of **Ir** reaches 1.6 x 10^{-3} M.[10] It is notable that the similar change is observed when temperature is changed. When the temperature dropped to 40 ^{o}C, both the critical temperature and the similar spectral shift of ^{1}LLCT are observed (Figure 3.6b). Therefore, the self-assembly can be rationalized by its dependency on both concentration of **Ir** and temperature of the solution as examined by abrupt changes at certain points and similar spectral shifts.

Finally, to see its potential application for photocatalytic hydrogen evolution, I investigated photoluminescence of **Ir** by changing temperature. Interestingly, sharp increase in photoluminescence is observed when the temperature dropped to 40 ^{o}C (Figure 3.7), which completely accords with the critical change in absorption spectra in Figure 3.6b. This change is attributed to the fluidity of sol form and the more facile non-radiative decay that occurs at higher temperature, thus confirming the superiority of gel to sol.[11] To far exploit the advantage of gel state over sol state, I tried to examine

photocatalytic hydrogen evolution with **Ir** and colloidal Pt catalyst in two states. However, the use of TEOA solution (WS sol) as a sacrificial reducing agent hampered the direct comparison between gel and sol due to its charge screening effect (Scheme 3.1). It was impossible to make both gel and sol by controlling the amount of NaCl because it already became gel as long as I use enough amount of TEOA for photocatalytic H_2-evolution. For this reason, I designed other experiments to confirm that gel state is favorable for photocatalysis. The first one was differing the amount of WS sol with same amount of **Ir**. I made two different systems as can be seen in Figure 3.8; one is a rigid gel on a glass at enough high concentration of **Ir** and the other is sol state at low concentration. As a result, the gel state showed far more photocatalytic activity and produced 11.5-times as many hydrogen during 40 h than the sol state (Figure 3.9a). Such high activity is originated from decrease in vibronic loss of **Ir** and efficient electron transfer from **Ir** to Pt colloid as their thermal movements are inhibited in gel state. The second method was to protonate **Ir** and induce precipitation, thus confirming the advantage of self-assembly. With colloidal Pt catalyst, I compared photocatalytic activity of **Ir** with protonated **Ir**. As a result, the former produced 8.8-times more hydrogen than the latter (Figure 3.9b). This is because protonated **Ir** randomly aggregate each other in water and its active site becomes limited only to its surface as depicted in Figure 3.10, which is unfavorable for photocatalysis. In contrast, **Ir** could self-assemble in water and form a nanosized column so that its active sites was far more numerous than the latter, thus showing more efficient photocatalytic hydrogen evolution.

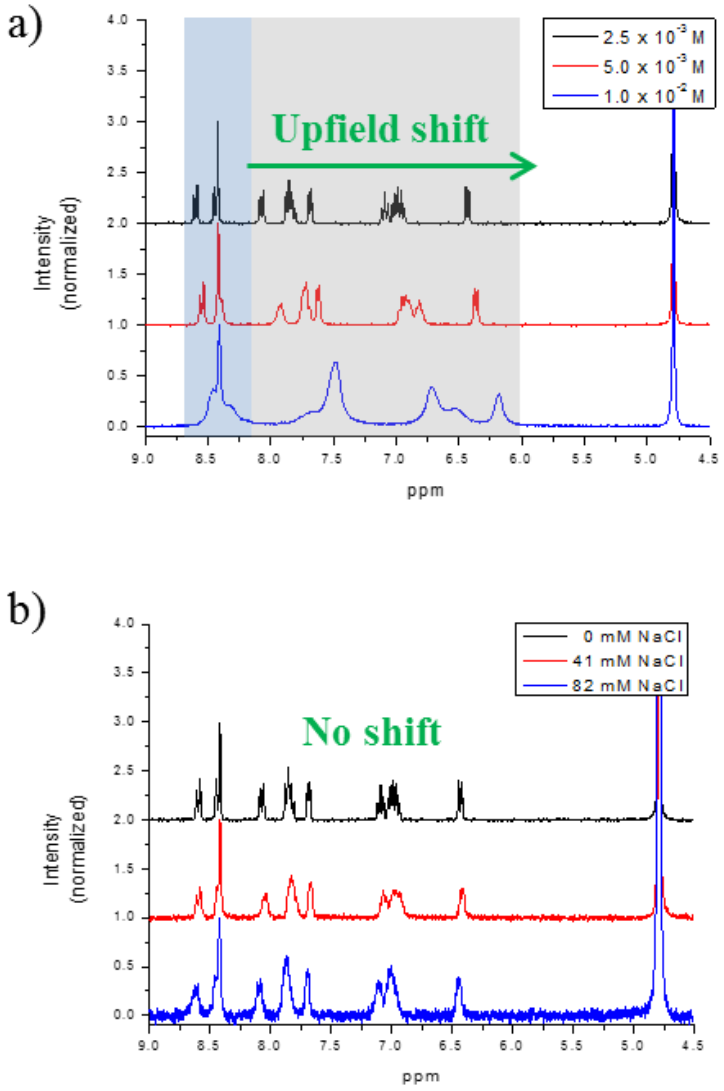

Figure 3.5 a) Up-field shift of phenylpyridine ligand with increasing concentration of **Ir**. b) There was no such shift when NaCl was added in 2.5 mM **Ir** solution.

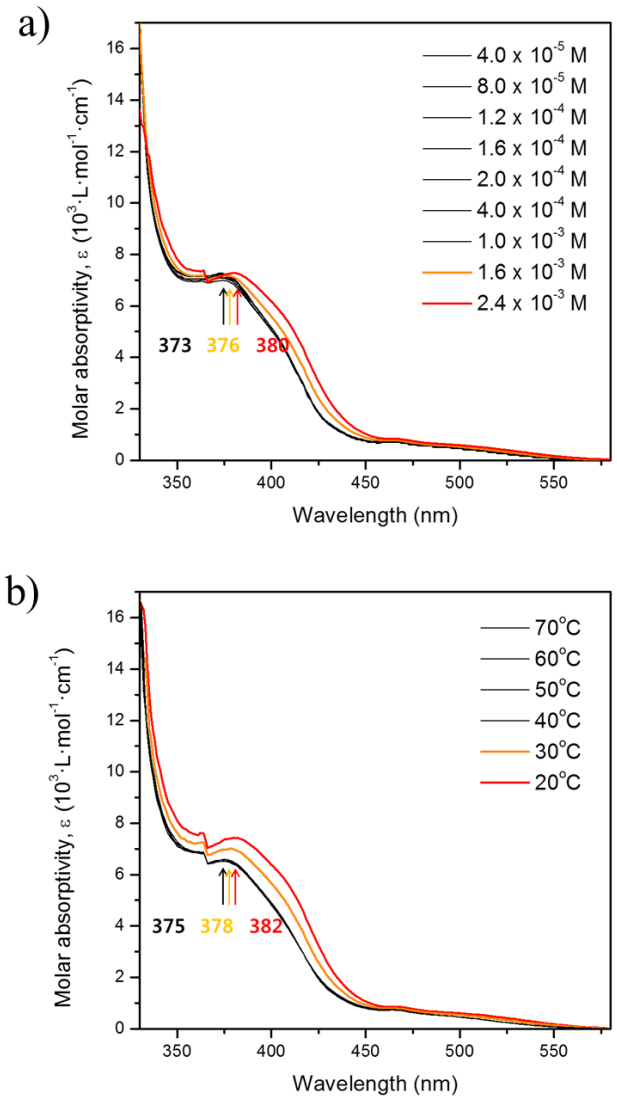

Figure 3.6 a) Spectral change in UV/Vis spectra with increasing concentration of **Ir** at room temperature. b) Spectral change in UV/Vis spectra with decreasing temperature of 2.4 mM **Ir** solution.

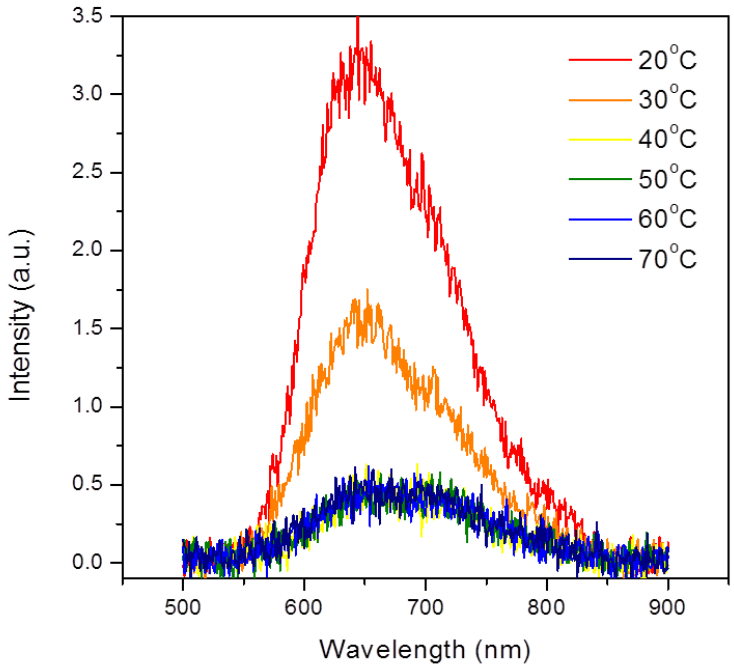

Figure 3.7 Increase in photoluminescence as vibronic loss of **Ir** is reduced in the gel state.

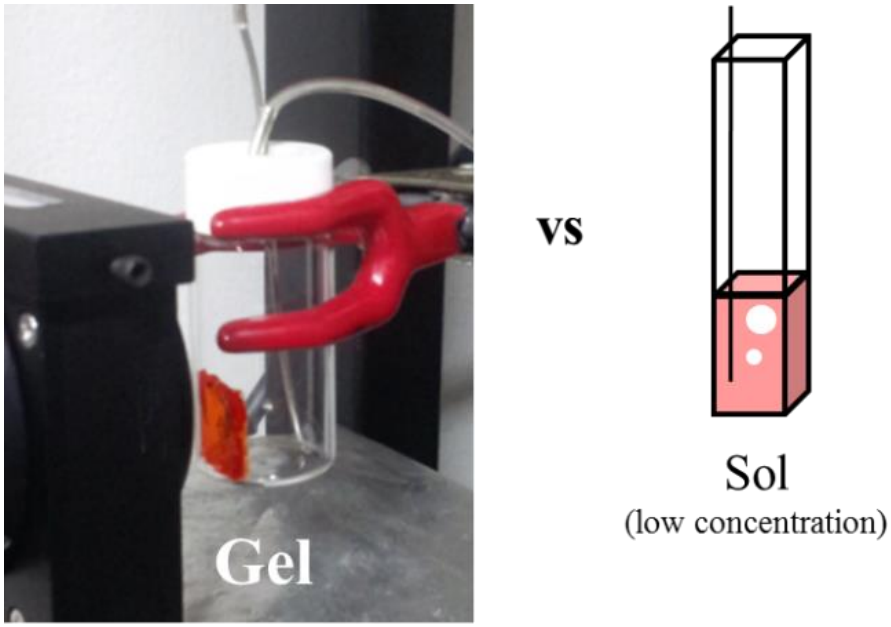

Figure 3.8 The pictures of **Ir** in gel (left) and sol (right) for photocatalytic H_2-evolution. Irradiation areas of each cells were same.

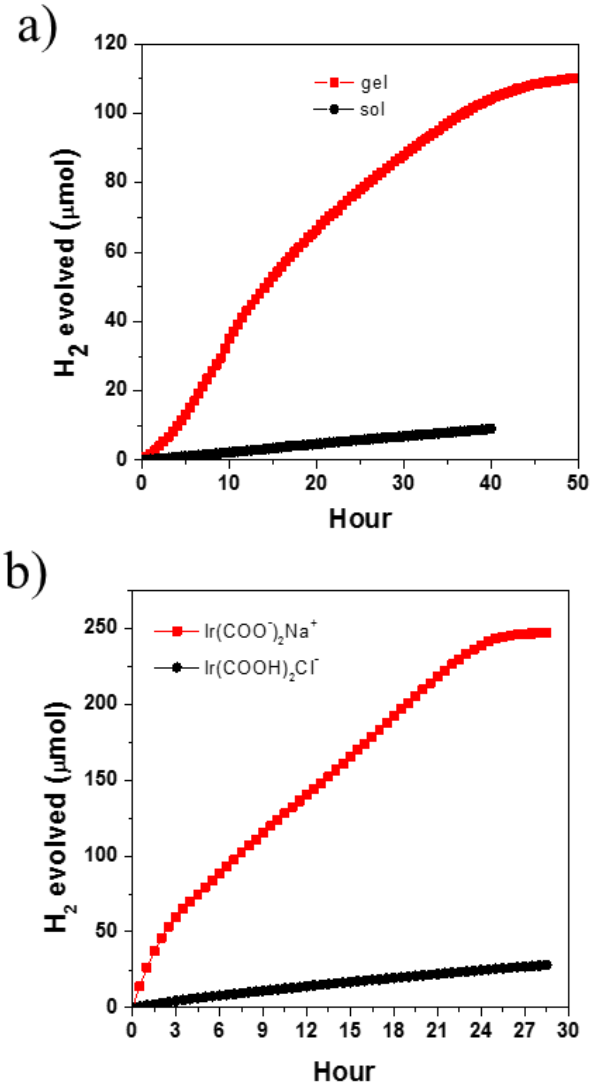

Figure 3.9 a) The comparison between gel state and sol state in photocatalytic hydrogen evolution. 11.5-times more hydrogen was evolved in gel state during the 40 h of photocatalysis. b) The comparison between **Ir** and protonated **Ir**. 8.5-times more hydrogen was evolved in **Ir** during 28.5 h due to its self-assembling ability.

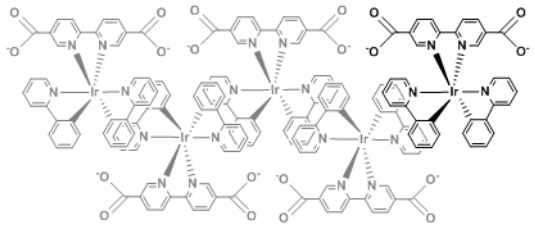

Deprotonated

vs

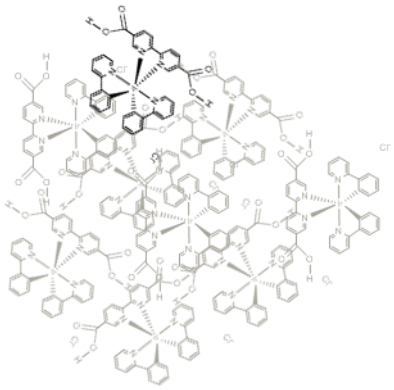

Protonated

Figure 3.10 The schematic description of how **Ir** (left) and protonated **Ir** (right) assemble themselves.

3.4 Conclusions

In summary, I designed an octahedral Ir(III) complex which can self-assemble in water and form hydrogel. In addition, its application for photocatalytic hydrogen evolution was investigated. The superiority of the gel state was supported by its enhanced photoluminescence and approximately 10-times more amount of hydrogen evolved than sol state. I believe that this research would open new doors in supramolecular chemistry and that this Ir(III) hydrogel would be widely used in the field of photochemistry.

3.5 References

1. Kim, J. H.; Lee, M.; Lee, J. S.; Park, C. B. *Angew. Chem.* **2012**, *51*, 517.
2. P. Jordan; P. Fromme; H. T. Witt; O. Klukas; W. Saenger; N. Krauss *Nature* **2001**, *411*, 909.
3. X. Yan; P. Zhu; J. Li *Chem. Soc. Rev.* **2010**, *39*, 1877.
4. T. Hasobe *Phys. Chem. Chem. Phys.* **2010**, *12*, 44.
5. Y. Liang; P. Guo; S. V. Pingali; S. Pabit; P. Thiyagarajan; K. M. Berlan; D. G. Lynn; *Chem. Commun.* **2008**, 6522.
6. Yadav, Y. J.; Heinrich, B.; De Luca, G.; Talarico, A. M.; Mastropietro, T. F.; Ghedini, M.; Donnio, B.; Szerb, E. I. *Adv. Opt. Mater.* **2013**, *1*, 844.
7. Weingarten, A. S.; Kazantsev, R. V.; Palmer, L. C.; McClendon, M.; Koltonow, A. R.; Samuel, A. P.; Kiebala, D. J.; Wasielewski, M. R.; Stupp, S. I. *Nat. Chem.* **2014**, *6*, 964.
8. Tamayo, A. B.; Alleyne, B. D.; Djurovich, P. I.; Lamansky, S.; Tsyba, I.; Ho, N. N.; Bau, R.; Thompson, M. E. *J. Am. Chem. Soc.* **2003**, *125*, 7377.
9. Huo, H.; Fu, C.; Harms, K.; Meggers, E. *J. Am. Chem. Soc.* **2014**, *136*, 2990.
10. Wu, S.-H.; Ling, J.-W.; Lai, S.-H.; Huang, M.-J.; Cheng, C. H.; Chen, I. C. *J. Phys. Chem. A* **2010**, *114*, 10339.
11. Tam, A. Y.-Y.; Wong, K. M.-C.; Wang, G.; Yam, V. W.-W. *Chem. Commun.* **2007**, 2028.

초 록

광촉매 물분해 수소생산을 위한 초분자 시스템에 관한 연구

인간 문명이 발전함에 따라 화석연료의 사용이 급격히 늘어났고 이는 지구 환경에 심각한 손상을 끼쳤다. 환경적인 문제와 더불어 사용할 수 있는 화석 연료의 매장량이 제한적이라는 문제점을 인식함에 따라 인간은 새로운 에너지원의 필요성을 절감하였다. 이러한 맥락에서 재생가능하고 친환경적인 에너지원을 생산하는 인공광합성 연구가 큰 관심을 불러일으키고 있다. 식물의 광합성은 물과 이산화탄소를 산소와 탄수화물로 변환시킴으로써 태양에너지를 화학에너지로 변환시키는 역할을 수행한다. 자연계의 광합성과는 달리 인공광합성은 물을 수소와 산소로 분리하여 수소를 에너지원으로 사용하는데 목적을 둔다 (* 이 논문에서는 편의상 인공광합성 연구를 물분해 분야로 제한하였다). 수소는 탄소를 전혀 포함하지 않아서 연소시 부산물로 물을 형성하고 이렇게 형성된 물은 수소를 생산하기 위한 자원으로 다시 사용될 수 있기 때문에 수소 에너지는 재사용가능하다. 최근에는 초분자적 접근을 이용하는 인공광합성 연구가 많은 관심을 받고 있다. 이는 초분자적 접근을 통해 단일 분자 상태에서는 가질 수 없는 새로운 특징을 구현할 수 있기 때문이다. 본 논문에서는 이러한 초분자

시스템을 광촉매 수소생산 반응에 활용한 두 연구를 보고하고자 한다.

2 단원에서는 최초로 광촉매 수소생산 반응 시 분자촉매의 자가치유가 가능한 시스템을 개발하는 연구를 보고하였다. 수소생산 분자촉매와 감광제를 포함하는 바이피리딘 (Bipyridine) 으로 구성된 UiO 타입의 금속유기구조체, Pt_n_Ir_BUiO 을 합성하여 광촉매 수소생산 반응을 진행시켰다. 이 금속유기구조체에 포함된 각 분자는 초분자적 시스템을 형성함으로써 각각의 고유한 성질을 유지할 수 있었다. $Pt_{0.1}$_Ir_BUiO 로 진행한 광촉매 수소생산 반응에서는 콜로이드가 전혀 형성되지 않았으며 아주 안정한 활성의 분자 광촉매반응을 보였다. 하지만 균일 조건에서 수행한 비교실험에서는 7.5 시간만에 콜로이드를 형성하였다. 이렇게 우수한 자가치유 능력을 보일 수 있는 이유는 diimine site 가 아주 가까이, 그리고 높은 밀도로 금속유기구조체 내의 수소생산 촉매를 둘러싸고 있기 때문이다.

3 단원에서는 물에서 자가조립이 가능한 이리듐 착체를 보고하였고 그 메커니즘을 제시하였다. 양쪽 친매성의 이리듐 착체를 고안하여 hydrophobic collapse 를 유도함으로써 물에서 이리듐 착체의 자가조립을 일으켰고, 염화나트륨을 첨가하여 전하 스크리닝 효과 (charge screening effect) 를 가함으로써 하이드로젤을 형성하도록 하였다. 또한, 이 하이드로젤이 광촉매 수소생산에 필요한 물, 감광제, 촉매, 그리고 희생시약을 모두 포함할 수 있고 수소를 효과적으로 생산할 수 있었다는 점에서 큰 중요성을 지닌다고 할 수 있다.

주요어: 인공광합성, 물분해, 광촉매 수소생산, 자가치유, 금속유기구조체, 자가조립, 이리듐(III) 하이드로젤
학 번: 2014-20535

List of Presentation

1. **Dongha Kim**, Dong Ryeol Whang, Soo Young Park, “Bifunctional Metal-Organic Framework for a Highly Robust Single-Component Photo-Hydrogen-Evolving Device”, **Faraday Discussions 176 (Next-Generation Materials for Energy Chemistry)**, Oct 27-29, 2014, Xiamen University, China.
2. **Dongha Kim**, Dong Ryeol Whang, Soo Young Park, “Self-Healing Bifunctional Metal-Organic Framework Functionalized with Photosensitizer and Catalyst: Robust Molecular Photocatalytic System for Water Reduction”, **International Conference on Photochemistry**, Jun 28-Jul 3, 2015, Jeju, Korea.